Contents lists available at ScienceDirect

Journal of Computational Physics

A remeshed vortex method for mixed rigid/soft body fluid–structure interaction

Yashraj Bhosale [a,1], Tejaswin Parthasarathy [a,1], Mattia Gazzola [a,b,c,*]

[a] *Mechanical Sciences and Engineering, University of Illinois at Urbana-Champaign, Urbana, IL 61801, USA*
[b] *National Center for Supercomputing Applications, University of Illinois at Urbana-Champaign, Urbana, IL 61801, USA*
[c] *Carl R. Woese Institute for Genomic Biology, University of Illinois at Urbana-Champaign, Urbana, IL 61801, USA*

ARTICLE INFO

ABSTRACT

We outline a 2D algorithm for solving incompressible flow–structure interaction problems for mixed rigid/soft body representations, within a consistent framework based on the remeshed vortex method. We adopt the one-continuum formulation to represent both solid and fluid phases on an Eulerian grid, separated by a diffuse interface. Rigid solids are treated using Brinkman penalization while an inverse map technique is used to obtain elastic stresses in the hyperelastic solid phase. We test our solver against a number of benchmark problems, which demonstrate physical accuracy and first to second order convergence in space and time. Benchmarks are complemented by additional investigations that illustrate the ability of our numerical scheme to capture essential fluid–structure interaction phenomena across a variety of scenarios involving internal muscular actuation, self propulsion, multi-body contact, heat transfer and rectified viscous streaming effects. Through these illustrations, we showcase the ability of our solver to robustly deal with different constitutive models and boundary conditions, solve disparate multi-physics problems and achieve faster time-to-solutions by sidestepping CFL time step restrictions.

1. Introduction

This paper presents a remeshed vortex method based formulation that captures essential two-way flow–structure interactions among multiple heterogeneous soft and rigid bodies immersed in an incompressible viscous fluid. We are motivated by the relevance of these effects in engineering and biology across scales [1–8], particularly in the context of soft robotics [9–11] and biolocomotion [12,13], where there exists an inextricable nexus between compliant mechanics, environmental interactions, control and behavior. Accurate and versatile solvers are then key to shed light on and dissect underlying mechanisms and design solutions, with potential applications beyond the above domains: from medicine, where compliant devices may be used to deliver drugs [14], to inertial microfluidics, where streaming effects [15–17] can be used for particle manipulation, or flow control for drag reduction or heat transfer enhancement. These problems are typically characterized by non-linear interfacial-driven coupled dynamics across disparate solid and fluid spatio-temporal scales, complex

---

solid morphologies and boundary conditions, and large elastic deformations. Because of these features, numerical studies in these settings have been traditionally challenging, and discoveries have been predominantly (although not exclusively) led by experiments, which are expensive and time consuming. Nonetheless, computational inroads have been made over the years. The resulting algorithms can be broadly classified into three major categories based on how the physical governing equations are discretized in the fluid and solid phases [18]. These discretization methods typically entail fully Lagrangian approaches, fully Eulerian approaches and mixed Lagrangian–Eulerian approaches.

In fully Lagrangian discretization methods, both fluid and solid phases' governing equations are discretized on particles advected by flow and solid velocity fields. Also known as meshless methods, popular members of this class include the reproducing kernel particle method (RKPM) [19] and smoothed-particle hydrodynamics (SPH) [20]. These methods present a number of attractive features such as simplified parallelization, good conservation properties and automatic local (r-) adaptivity [21]. At the same time they are limited in their ability to treat boundary conditions, are accompanied by higher algorithmic costs compared to traditional grid based methods [21,22], and may incur particle distortion effects that can severely impair accuracy.

On the other side of the spectrum lies the fully Eulerian discretization methods in which the governing equations for both the phases are discretized on a fixed Eulerian grid or mesh, with the solid–fluid boundary usually tracked using implicit techniques such as level set [23] and volume of fluid (VOF) [24] method. This category has seen recent developments through the use of reference map technique coupled with level sets [25], and Cauchy–Green tensor advection coupled with VOF [26], for the treatment of elastic solids immersed in viscous fluids. These approaches are typically implemented through finite differences [26] or finite volumes [18]. These methods have been shown to successfully capture flow past elastic bodies, self-propulsion, solid-solid contact physics, or haemodynamics among others [18,25–28], and offer a number of attractive features such as cost effectiveness due to the fixed mesh, straightforward evaluation of operators and simplicity in parallelization. At the same time, they are hampered by difficulties in resolving slender structures, treating far field boundary conditions and face advection-based CFL time step restrictions.

Finally, the most commonly used, diverse and historically significant class is the mixed Lagrangian–Eulerian discretization approach, where the solid phase equations are discretized on a Lagrangian grid while the fluid phase equations are discretized on a fixed Eulerian mesh. This class can be divided into two major sub classes, namely partitioned domain methods and monolithic domain methods. Partitioned domain methods are characterized by separate meshes/solution spaces for the solid and fluid phases, and typically include members such as arbitrary Lagrangian-Eulerian (ALE) approach [29] and deforming-spatial-domain/stabilized-space-time approach (DST/SST) [30], within the context of finite element methods. These established methods, while mathematically involved, possess rigorous convergence properties and have proven useful in a number of applications, from (bio-)propulsion [31] to cardiovascular modeling [32] or aerodynamics [33]. Yet, their parallel implementation might be challenging given their partitioned approach, while also requiring generation of a new grid every few time steps to avoid computational element distortion, rendering them computationally expensive for highly deforming elastic solids [34]. Monolithic domain methods instead solve a single set of governing equations over the entire domain with the solid–fluid coupling boundary conditions formulated as appropriate forcing terms. Well known members include immersed methods [35] (immersed boundary [36–40], immersed finite element [41–44] and immersed interface [45] methods) and fictitious domain methods [46–48]. These methods are known for their versatility and have been widely used to study flow past complex geometries [36,37], bio-mimetic propulsion [39,42,43,48–50], hemodynamics [36,44] and flow induced vibration [39,40,47,50]. However, these methods also face advection-based CFL time step restrictions, as well as difficulties in achieving higher-order convergence. We note that while the classification above serves as a useful, high level guidance, methods might straddle across categories. For a more detailed classification, we refer the reader to the recent paper of Jain et al. [18].

An alternative approach known as remeshed vortex method has developed considerably in the past decade to mitigate advection time step restrictions, while offering high accuracy. It discretizes the solid phase equations on a fixed Eulerian mesh, while the fluid equations alternate between a Lagrangian and Eulerian discretization to solve for the velocity–vorticity formulation of the momentum equation (as opposed to the velocity–pressure formulation used in other methods) [51–55]. It carries over a number of attractive features from Lagrangian and Eulerian methods, including guaranteed convergence, stability, accuracy, compact support of vorticity leading to automatic local (r-)adaptivity, natural treatment of far field boundary conditions, ability to model complex solid morphologies, relaxed advection stability conditions, and computational economy rivaling traditional grid based methods [51–60,12,61,62]. This makes it a versatile method to capture the presence of unsteady, complex bodies [58–60,62] across scales [61,63,64], to deal with contact physics [57], multiphase [65] and compressible flows [66,67], in 2D as well as in 3D [60,68,69]. Yet, despite this versatility, little effort has been made to capitalize on these advantages to solve the strongly coupled equations of motion between multiple heterogeneous soft and rigid bodies and surrounding fluid.

In this work, we provide this crucial contribution. Specifically, we combine inverse map technique and Brinkman penalization within a consistent and seamless one-fluid formulation to account for full two-way coupling between an incompressible viscous fluid and multiple, heterogeneous rigid and elastic bodies. This approach combines the attractive features of vortex methods, with the ones of the inverse map technique, namely, straightforward solid stress evaluation, stability and convenient solid–fluid interface tracking based on the same machinery of the Brinkman penalization. While previous

attempts employed simplified 1D formulations leveraging the slenderness of thin elastic structures [40,70], our method solves for bulk elasticity and enables the simulation of arbitrarily shaped 2D soft bodies. Through numerous benchmarks and illustrations, we then demonstrate the accuracy, robustness and versatility of our solver across multiphysics scenarios, boundary conditions, constitutive and actuation models.

The work is organized as follows: governing equations and the various techniques used to solve them are described in Section 2 and Section 3, respectively; the proposed algorithm and the numerical discretization is detailed in Section 4; rigorous benchmarking and convergence analysis is presented in Section 5; versatility and robustness of the solver is illustrated through a variety of multifaceted cases in Section 6; finally, concluding remarks are provided in Section 7.

2. Governing equations

In this section, we present the complete set of governing equations and constitutive laws that define the dynamics of multiple rigid/elastic bodies immersed in a viscous fluid.

2.1. Governing equations for solids and fluids

We consider a two-dimensional domain Σ physically occupied by a viscous fluid and rigid and elastic bodies. We denote with $\Omega_{e,i}$ & $\partial\Omega_{e,i}$, $i = 1, \ldots, N_e$ and $\Omega_{r,j}$ & $\partial\Omega_{r,j}$, $j = 1, \ldots, N_r$ the support and boundaries of the elastic and rigid solids, respectively. Denoting $\overline{\Omega} = \overline{\Omega_{e,i}} \cup \overline{\Omega_{r,j}}$ to be the region occupied by solid material, the fluid then occupies the region $\Sigma - \overline{\Omega}$.

Linear and angular momentum balance of elastic solid and fluid domains (for Eulerian differential volumes $d\boldsymbol{x}$), result in the Cauchy momentum equation

$$\frac{\partial \boldsymbol{v}}{\partial t} + \nabla \cdot (\boldsymbol{v} \otimes \boldsymbol{v}) = -\frac{1}{\rho}\nabla p + \boldsymbol{b} + \frac{1}{\rho}\nabla \cdot \boldsymbol{\sigma}', \quad \boldsymbol{x} \in \Sigma \setminus \Omega_{r,j} \tag{1}$$

where $t \in \mathbb{R}^+$ represents time, $\boldsymbol{v} : \Sigma \times \mathbb{R}^+ \mapsto \mathbb{R}^2$ represents the velocity field, ρ denotes material density, $p : \Sigma \times \mathbb{R}^+ \mapsto \mathbb{R}$ represents the hydrostatic pressure field, $\boldsymbol{b} : \Sigma \times \mathbb{R}^+ \mapsto \mathbb{R}^2$ represents a conservative volumetric body force field and $\boldsymbol{\sigma}' : \Sigma \times \mathbb{R}^+ \mapsto \mathbb{R}^2 \otimes \mathbb{R}^2$ is the deviatoric Cauchy stress tensor field. As a convention, the prime symbol $'$ on a tensor $\boldsymbol{A}$ denotes it is deviatoric, i.e. $\boldsymbol{A}' := \boldsymbol{A} - \frac{1}{2}tr(\boldsymbol{A})\boldsymbol{I}$, with $\boldsymbol{I}$ representing the tensor identity and $tr(\cdot)$ representing the trace operator. We assume that all fields defined above are sufficiently smooth in time and space. Incompressibility of the fluid and elastic domains is kinematically enforced through

$$\nabla \cdot \boldsymbol{v} \equiv 0, \quad \boldsymbol{x} \in \Sigma. \tag{2}$$

The fluid and elastic solid phases interact exclusively via boundary conditions, imposing continuity in velocities (no-slip) and traction forces at all fluid–elastic solid interfaces

$$\boldsymbol{v} = \boldsymbol{v}_f = \boldsymbol{v}_{e,i}, \quad \boldsymbol{\sigma}_f \cdot \boldsymbol{n} = \boldsymbol{\sigma}_{e,i} \cdot \boldsymbol{n}, \quad \boldsymbol{x} \in \partial\Omega_{e,i} \tag{3}$$

where $\boldsymbol{n}$ denotes the unit outward normal vector at the interface $\partial\Omega_{e,i}$. Here $\boldsymbol{v}_f$ and $\boldsymbol{v}_{e,i}$ correspond to the interfacial velocities in the fluid and i^{th} elastic body, respectively, while $\boldsymbol{\sigma}_f$ and $\boldsymbol{\sigma}_{e,i}$ correspond to the interfacial Cauchy stress tensor in the fluid and i^{th} elastic body, respectively.

In the region $\Omega_{r,j}$, $j = 1, \ldots, N_r$ occupied by rigid solids, the velocities are kinematically restricted to rigid body modes of pure translation and rotation. Hence, all rigid bodies interact with the fluid domain only via the no-slip boundary condition

$$\boldsymbol{v} = \boldsymbol{v}_f = \boldsymbol{v}_{r,j} = \underbrace{\dot{\boldsymbol{x}}_{\text{cmr},j}}_{\text{translation}} + \underbrace{\dot{\theta}_{r,j} \times (\boldsymbol{x} - \boldsymbol{x}_{\text{cmr},j})}_{\text{rotation}}, \quad \boldsymbol{x} \in \partial\Omega_{r,j} \tag{4}$$

where $\boldsymbol{v}_{r,j}$ is the rigid velocity field, $\boldsymbol{x}_{\text{cmr},j}$ is the center of mass (COM) position, and $\theta_{r,j}$ is the angular orientation about this COM of the jth rigid body.

2.2. Constitutive laws for fluid and elastic solids

To close the above set of equations (Eqs. 1 to 4) and determine the system dynamics, it is necessary to specify the form of internal material stresses, i.e. their constitutive laws. Here, we discuss specific modeling choices for the deviatoric Cauchy stress tensor $\boldsymbol{\sigma}'$ of Eq. 1, across the different phases.

The fluid is assumed to be Newtonian, isotropic and incompressible with density ρ_f, dynamic viscosity μ_f and kinematic viscosity $\nu_f = \mu_f / \rho_f$. As such, the deviatoric Cauchy stress is comprised of the purely viscous term

$$\boldsymbol{\sigma}_f{}' := 2\mu_f \boldsymbol{D}' \tag{5}$$

where $\boldsymbol{D}'$ is the strain rate tensor $\frac{1}{2}\left(\nabla \boldsymbol{v} + \nabla \boldsymbol{v}^T\right)$.

Next, we assume that the elastic solid is isotropic, incompressible, has constant density ρ_e and exhibits both elastic and viscous (or *visco-elastic*) behavior. Then the deviatoric Cauchy stress can be modeled as

$$\boldsymbol{\sigma}_e{}' := 2\mu_e \boldsymbol{D}' + \boldsymbol{\sigma}'_{he} \tag{6}$$

where μ_e represents the dynamic viscosity of the solid material (indicative of internal damping effects) and $\boldsymbol{D}'$ is the strain rate tensor. For convenience, we can also define the kinematic viscosity of the solid $\nu_e = \mu_e / \rho_e$.

The term $\boldsymbol{\sigma}'_{he}$ is the hyperelastic contribution to the solid stress tensor. We describe it here through the generalized Mooney–Rivlin model [26,71], developed to capture finite-strain elastomeric and biological tissue material responses. We then consider an elastic solid in a convective coordinate system evolving with time t. At $t = 0$, the solid is in its initial, stress-free configuration. A material point location within the solid is denoted by $\boldsymbol{X} \in \Omega_e^0 \subset \mathbb{R}^2$. Due to external or internal forces and couples, the solid displaces and distorts in physical space $\boldsymbol{x} \in \Omega_e(t) \subset \mathbb{R}^2$ for $t > 0$. Phenomenologically, the stress field $\boldsymbol{\sigma}'_{he}$ is a function of the displacement $\boldsymbol{u} = \boldsymbol{x} - \boldsymbol{X}$ (or equivalently strain) of a solid material point, and arises from the strain energy density function W stored in the solid due to deformations. This is equivalent to $\boldsymbol{\sigma}'_{he}$ being only dependent on the deformation gradient $\boldsymbol{F} := \partial \boldsymbol{x}/\partial \boldsymbol{X}$ and not on $\boldsymbol{x}$ itself (intuitively, purely rigid body motions cause no stress). Galilean invariance dictates that this dependence on $\boldsymbol{F}$ occurs only through the rotationally-invariant left $\boldsymbol{B} := \boldsymbol{F} \boldsymbol{F}^T$ or right $\boldsymbol{C} := \boldsymbol{F}^T \boldsymbol{F}$ Cauchy–Green deformation tensors. Without loss of generality, the strain energy density W can then be modeled as a function of $\boldsymbol{C}$ only

$$W(\boldsymbol{C}) := c_1\left(\widetilde{I}_{\boldsymbol{C}} - 2\right) + c_2\left(\widetilde{II}_{\boldsymbol{C}} - 2\right) + c_3\left(\widetilde{I}_{\boldsymbol{C}} - 2\right)^2 \tag{7}$$

where c_1, c_2 and c_3 are material constants, and $\widetilde{I}_{\boldsymbol{C}}$ and $\widetilde{II}_{\boldsymbol{C}}$ are the reduced invariants of $\boldsymbol{C}$ defined as

$$\widetilde{I}_{\boldsymbol{C}} := \frac{I_{\boldsymbol{C}}}{III_{\boldsymbol{C}}^{1/3}}, \quad \widetilde{II}_{\boldsymbol{C}} := \frac{II_{\boldsymbol{C}}}{III_{\boldsymbol{C}}^{2/3}} \tag{8}$$

through the matrix invariants

$$I_{\boldsymbol{C}} := tr(\boldsymbol{C}), \quad II_{\boldsymbol{C}} := \frac{1}{2}\left(I_{\boldsymbol{C}}^2 - tr(\boldsymbol{C} \cdot \boldsymbol{C})\right), \quad III_{\boldsymbol{C}} := det(\boldsymbol{C}) \tag{9}$$

with $det(\cdot)$ representing the determinant operator. By combining Eqs. 7 to 9 and recalling that for incompressible hyperelastic materials

$$\boldsymbol{\sigma}'_{he} = \left(2\boldsymbol{F}\frac{\partial W(\boldsymbol{C})}{\partial \boldsymbol{C}}\boldsymbol{F}^T\right)' \tag{10}$$

the final expression for the Cauchy stress reduces to

$$\begin{aligned}
\boldsymbol{\sigma}'_{he} &= \left(2\boldsymbol{F}\left[c_1\frac{\partial \widetilde{I}_{\boldsymbol{C}}}{\partial \boldsymbol{C}} + c_2\frac{\partial \widetilde{II}_{\boldsymbol{C}}}{\partial \boldsymbol{C}} + c_3(\widetilde{I}_{\boldsymbol{C}} - 2)\frac{\partial \widetilde{I}_{\boldsymbol{C}}}{\partial \boldsymbol{C}}\right]\boldsymbol{F}^T\right)' \\
&= \left(2c_1\boldsymbol{B} + 2c_2(tr(\boldsymbol{B})\boldsymbol{B} - \boldsymbol{B} \cdot \boldsymbol{B}) + 4c_3(tr(\boldsymbol{B}) - 2)\boldsymbol{B}\right)'.
\end{aligned} \tag{11}$$

For small deformations, the coefficients $2(c_1 + c_2)$ represent G, the shear modulus of the solid, and c_3 is loosely related to the bulk modulus (K) of the material. Finally, if we set $c_2 = c_3 = 0$ and $2c_1 = G$ in Eq. 11, we recover the Cauchy stress corresponding to a neo-Hookean material

$$\boldsymbol{\sigma}'_{he} = G\boldsymbol{B}'. \tag{12}$$

We note that the above linear relation between $\boldsymbol{\sigma}'_{he}$ and $\boldsymbol{B}'$ does not amount to a linear stress-strain response as in perfectly elastic materials, because $\boldsymbol{B} := \boldsymbol{F}\boldsymbol{F}^T$ contains strain non-linearities which account for Galilean invariance. Indeed, the neo-Hookean model has been developed to capture non-linear stress-strain behaviors, but differently from the generalized Mooney–Rivlin model, it does so to a lesser degree of accuracy and generality. Nonetheless, due to its popularity and for comparison purposes we consider here the neo-Hookean model as well.

3. Methodology

With the fundamental governing equations and boundary conditions established, we now present the techniques used to solve these equations. Our approach builds upon the method developed in Gazzola et al. [58] for rigid body flow–structure simulations, but crucially augments it to account for the full two-way coupling between fluids, rigid and elastic bodies, in a seamless fashion. For this, we use the inverse map technique to track solid deformations, couple it with a hyperelastic constitutive model and adopt the one continuum formulation to solve the coupling problem in a unified remeshed vortex methods framework.

3.1. Remeshed vortex method

We consider the velocity–vorticity formulation of the 2D Cauchy momentum equation Eq. 1

$$\frac{\partial \omega}{\partial t} + \nabla \cdot (\boldsymbol{v}\omega) = \underbrace{-\frac{\nabla \rho}{\rho^2} \times \nabla p + \frac{1}{\rho}\nabla \times \nabla \cdot \boldsymbol{\sigma}' + \nabla \times \boldsymbol{b}}_{\text{RHS}} \tag{13}$$

where $\omega : \Sigma \times \mathbb{R}^+ \mapsto \mathbb{R} := \nabla \times \boldsymbol{v}$ represents the vorticity field. Vortex methods discretize ω by means of particles, characterized by their position $\boldsymbol{x}_p$, volume V_p and strength corresponding to the vorticity integral $\Gamma_p = \int_{V_p} \omega d\mathbf{x}$. The advection of particles and quantities they represent is performed in a Lagrangian fashion where they move according to the velocity field $\boldsymbol{v}$ with strengths Γ_p evolving in accordance with RHS of Eq. 13.

$$\frac{d\boldsymbol{x}_p}{dt} = \boldsymbol{v}(\boldsymbol{x}_p, t); \quad \frac{d\Gamma_p}{dt} = [\text{RHS}]_{V_p} \tag{14}$$

In order to avoid Lagrangian distortion [56], a remeshing approach is used. Particle strengths and locations are interpolated onto an underlying regular grid at the end of each step using a high order, moment preserving interpolation scheme [58]. This approach enables a number of favorable features: use of fast differential operators to evaluate RHS terms, use of efficient Fourier transforms for solving Poisson equations, numerical accuracy, relaxed stability condition for advection, compact vorticity support and software scalability [58,61,65,68,69,72].

3.2. Eulerian representation of interfaces using level sets

All fluid–solid interfaces in our algorithm $\partial \Omega_i$ are captured using separate level set [23] functions $\phi_i : \Sigma \times \mathbb{R}^+ \mapsto \mathbb{R}$ such that

$$\partial \Omega_i = \{\boldsymbol{x} \in \Sigma \mid \phi_i(\boldsymbol{x}, t) = 0\}.$$

These interfaces are then advected by the velocity field $\boldsymbol{v}(\boldsymbol{x}, t)$

$$\frac{d\phi_i}{dt} + \boldsymbol{v} \cdot \nabla \phi_i = 0 \tag{15}$$

starting from their initial location $\phi_i(\boldsymbol{x}, 0) = \phi_i^0(\boldsymbol{x})$, with ϕ_i^0 being a signed-distance function at time $t = 0$. The outward normal at the interface is computed [23] as $\boldsymbol{n}_i = \nabla \phi_i / \|\nabla \phi_i\|$.

3.3. Brinkman penalization

In order to account for the presence of rigid bodies, we employ the Brinkman penalization technique [73,74]. In the penalization technique, the flow velocity field is extended inside the rigid bodies, and the Cauchy momentum equation (Eq. 1) is equipped with an additional forcing term, to approximate the no-slip boundary conditions of Eq. 4 (see [75] for detailed proofs).

$$\frac{\partial \boldsymbol{v}_\lambda}{\partial t} + \nabla \cdot (\boldsymbol{v}_\lambda \otimes \boldsymbol{v}_\lambda) = -\frac{1}{\rho}\nabla p_\lambda + \frac{1}{\rho}\nabla \cdot \boldsymbol{\sigma}'_\lambda + \boldsymbol{b} + \lambda \sum_i H(\phi_{r,j})(\boldsymbol{v}_{r,j} - \boldsymbol{v}), \quad \nabla \cdot \boldsymbol{v}_\lambda = 0, \quad \boldsymbol{x} \in \Sigma \tag{16}$$

where $\lambda \gg 1$ is the penalization factor, $H(\cdot)$ denotes the Heaviside function, $\phi_{r,j}$ corresponds to the level set which captures the interface of the jth rigid body and a subscript λ denotes the penalized fields satisfying the Brinkman–Cauchy Eq. 16. This penalization factor λ can be chosen arbitrarily and directly controls the error in the penalized solution, bounded by $\|\mathbf{v} - \mathbf{v}_\lambda\| \leq C\lambda^{-1/2} \|\mathbf{v}\|$ [73,76]. For a detailed discussion, the reader is referred to [58].
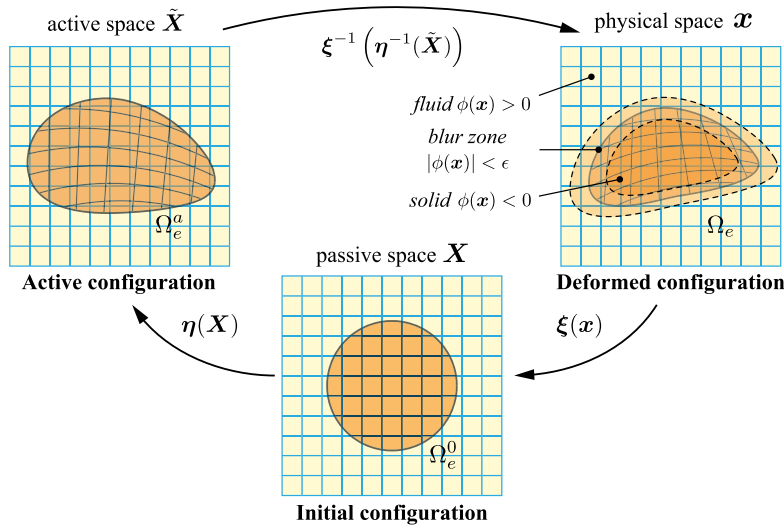
Fig. 1. Schematic of a deforming elastic solid, showing the initial (Ω_e^0, represented by the passive space X), deformed (Ω_e, represented by the physical space x) and active (Ω_e^a, represented by the active space $\tilde{X}$) configurations and their mappings ξ and η. This bijective map allows us to transform between the three spaces (and hence their respective configurations). Yellow squares (with blue borders) indicate the background (discrete) Eulerian grid occupied by the fluid phase. Orange (with black lines) indicate the Lagrangian grid of the solid, which we project onto the background Eulerian grid. Additionally, upon discretization, the zero level set contour ($\phi(x) = 0$) of the solid is used to distinguish the fluid $\phi(x) > 0$ and solid $\phi(x) < 0$ phases, with mixed solid–fluid behavior in the blur-zone $|\phi(x)| < \epsilon$. (For interpretation of the colors in the figure(s), the reader is referred to the web version of this article.)

3.4. Projection approach

While the no-slip condition is enforced via penalization, the feedback from the fluid to the rigid bodies is captured using a projection approach and Newton's equations of motion

$$m_{r,j}\ddot{x}_{cmr,j} = F_{r,j}^H ; \quad J_{r,j}\ddot{\theta}_{r,j} = M_{r,j}^H \tag{17}$$

where $m_{r,j}$, $J_{r,j}$, $F_{r,j}^H$ and $M_{r,j}^H$ are, respectively, mass and moment of inertia of the jth rigid body, and hydrodynamic force and moment acting on it. At the start of each time step, the flow is let to evolve freely over the entire domain as if the rigid bodies were not there (i.e. the velocity field is evolved inside the bodies themselves). The resulting new velocity field violates the rigid motion of the body, as well as its no-slip condition. To recover correct motion and physical consistency, we project the evolved velocity onto a subspace comprised of only rigid (translational and rotational) modes. Such a projection is possible because the extra momentum flux that the body obtains from the freely evolved flow correctly captures the feedback from the fluid onto the body over the time step. After the rigid components of motion are recovered, they are used to penalize the velocity field, thus regaining physical consistency, and to advect the level sets. Therefore the interplay between projection and penalization allows to achieve flow–structure coupling without the explicit use of forces and torques. A detailed proof can be found in [75]. We conclude this section by noting that, in this case, the level set advection equation Eq. 15 can be semi-analytically solved, so as to directly impose

$$\phi_{r,j}(x, t) = \phi_i^0(x; x_{cmr,j}(t), \theta_{r,j}(t)).$$

3.5. Inverse map technique

To capture the elastic solid phase dynamics, we need to compute the deformation gradient tensor F in time. For this, two approaches may be used: advect the Lagrangian tensor F directly on a fixed grid or *remember* the origin X of a material point for all points in the current solid phase x and then compute the deformation gradient per $F := \partial x / \partial X$. We choose the second approach, and adopt the inverse map technique described below to compute F in a purely Eulerian fashion—for a detailed comparison between these approaches the reader is referred to [77]. This methodology has been (re)discovered many times across different communities [77–82] and is known by several names (inverse map [78], initial-point set [83], LSPC [79], original-coordinates [80], backward-characteristics [84], reference-map [77], reference-coordinates [82]). In the context of flow–structure interaction, it has found use in simulating elastic membranes submerged in incompressible flow [81,84], and recently it has been extended to incompressible two-dimensional solids, using the p–v formulation of the Navier–Stokes equation and finite volumes and differences [18,85].

To illustrate the inverse map technique, we first consider an elastic solid in a convective coordinate system (Fig. 1), evolving with time t. We start at $t = 0$ with the solid in its initial configuration, and denote a material point within the

solid by $\boldsymbol{X} \in \Omega_e^0 \subset \mathbb{R}^2$. Due to external forces, the solid displaces and distorts occupying the physical space $\boldsymbol{x} \in \Omega_e(t) \subset \mathbb{R}^2$ at $t > 0$. Because of material conservation, each point in Ω_e must have originated from a univocal point in Ω_e^0, i.e. there must exist a mapping $\boldsymbol{\xi} : \Omega_e \times \mathbb{R}^+ \mapsto \Omega_e^0$ such that $\boldsymbol{\xi}(\boldsymbol{x}, t) := \boldsymbol{X}$ with $\boldsymbol{\xi}$ being sufficiently smooth (at least $\mathcal{C}^1$ continuous), and bijective. This diffeomorphic mapping is referred to as the inverse map. Physically, it denotes the origin of the material point occupying Eulerian position $\boldsymbol{x}$ at time t. From the definition above, $\boldsymbol{\xi}$ is invariant for a material point (its origin is always the same), implying that the material derivative of $\boldsymbol{\xi}$ is identically zero. For an incompressible medium, this yields

$$\frac{\partial \boldsymbol{\xi}}{\partial t} + \boldsymbol{v} \cdot \nabla \boldsymbol{\xi} = \boldsymbol{0}, \quad \boldsymbol{\xi}(\boldsymbol{x}, 0) = \boldsymbol{x} = \boldsymbol{X} \tag{18}$$

Therefore, the origin of a material point can be remembered as a field variable governed by a pure advection evolution law.

The inverse map enables the computation of solid stresses in a straightforward manner via $\boldsymbol{F}$ (Section 2.2). Since $\boldsymbol{\xi}(\boldsymbol{x}, t) := \boldsymbol{X}$, then $\partial \boldsymbol{X}/\partial \boldsymbol{x} = \nabla \boldsymbol{\xi}$ and hence $\boldsymbol{F} := \partial \boldsymbol{x}/\partial \boldsymbol{X} = (\nabla \boldsymbol{\xi})^{-1}$, where the gradient ∇ is a purely Eulerian operator in physical space. Here the existence of $(\nabla \boldsymbol{\xi})^{-1}$ assumes bijectivity of $\boldsymbol{\xi} \, \forall t > 0$, i.e. the inverse map does not *fold* over itself. Since the fluid zone is characterized by high shear rates $\|\boldsymbol{v}\|$, $\boldsymbol{\xi}$ may fold over. To reduce this risk we only define $\boldsymbol{\xi}$ inside the solid phase which has characteristic low $\|\boldsymbol{v}\|$ values for any physical choice of W. In all our numerical simulations, we found that this choice prevented $\boldsymbol{\xi}$ to fold and preserved its bijectivity.

An elastic solid material may undergo plastic effects or may be activated internally (mimicking the effect of muscles [86,87]). In this case, one can define an additional *active* configuration $\Omega_e^a(t) \subset \mathbb{R}^2$ (Fig. 1) that the solid tries to approach to minimize its internal strain energy. We then define this active configuration and introduce an additional diffeomorphic mapping $\boldsymbol{\eta} : \Omega_e^0 \times \mathbb{R}^+ \mapsto \Omega_e^a$ such that $\boldsymbol{\eta}(\boldsymbol{X}, t) := \tilde{\boldsymbol{X}}$ where $\tilde{\boldsymbol{X}}$ indicates a material point $\in \Omega_e^a$. Here $\boldsymbol{\eta}$ can be directly specified (in the case of muscular activation) or evolved separately under its own specifics (such as in elasto-plasticity). By composition of diffeomorphisms, we can obtain another diffeomorphic mapping relating active and physical space $\tilde{\boldsymbol{X}} = \boldsymbol{\eta}(\boldsymbol{\xi}(\boldsymbol{x}, t), t) \Longleftrightarrow \boldsymbol{x} = \boldsymbol{\xi}^{-1}\left(\boldsymbol{\eta}^{-1}\left(\tilde{\boldsymbol{X}}, t\right), t\right)$. Then the total deformation gradient $\boldsymbol{F}$ is $\partial \boldsymbol{x}/\partial \tilde{\boldsymbol{X}} = \partial \boldsymbol{x}/\partial \boldsymbol{X} \cdot \partial \boldsymbol{X}/\partial \tilde{\boldsymbol{X}} = (\nabla \boldsymbol{\xi})^{-1} \cdot (\nabla \boldsymbol{\eta})^{-1} = (\nabla \boldsymbol{\eta} \cdot \nabla \boldsymbol{\xi})^{-1}$ is fed into the constitutive model (Eq. 11). This representation leads to a neatly compartmentalized machinery, in which a variety of effects can be nested. We will demonstrate its use in Section 6.4, to simulate self-propelled, active and soft swimmers.

We equip each elastic body i with its own $\boldsymbol{\xi}_i$ field. This field can then be used to detect the interface $\partial \Omega_{e,i}$, by simply substituting Eq. 18 in Eq. 15 to obtain

$$\phi_{e,i}(\boldsymbol{x}, t) = \phi_i^0(\boldsymbol{\xi}_i(\boldsymbol{x}, t)),$$

which is beneficial as we now do not need to evolve ϕ in time, preserving consistent interface positions between $\boldsymbol{\xi}_i$ and ϕ_i at all times. As a final remark, we note that for all incompressible elastic materials $\det(\boldsymbol{F}) \equiv \det(\nabla \boldsymbol{\xi}) \equiv \det(\nabla \boldsymbol{\eta}) \equiv 1$. In our case this is identically satisfied as a byproduct of the velocity field incompressibility (Eq. 2, see Jain et al. [18] for a proof).

3.6. Solid–fluid representation

With well defined governing equations, boundary conditions, constitutive laws and interface characterization, we now proceed to describe the solid–fluid representation used in our algorithm. To solve the coupling problem, we adopt a conservative mixture model based on the one-fluid formulation used in two-phase flows, also known as the *one-continuum* formulation [88]. In this formulation, both solids and fluid share the same solution space and a monolithic velocity field (see Fig. 1). In the elastic solid regions, the Cauchy stress is computed using the solid constitutive law (Eq. 6), while in the fluid zone the stress is computed using the fluid constitutive law (Eq. 5). Then, a Heaviside function is used to smoothly blend the stresses and compute the monolithic Cauchy stress

$$\boldsymbol{\sigma}' = \sum_i H(\phi_{e,i}) \, \boldsymbol{\sigma}'_{e,i} + \left(1 - \sum_i H(\phi_{e,i})\right) \boldsymbol{\sigma}'_f \tag{19}$$

where $\sigma'_{e,i}$ and $\phi_{e,i}$ are, respectively, the solid stress tensor and level set (defining the geometry) of the ith elastic body. Similarly, one can define a monolithic density field

$$\rho = \sum_i H(\phi_{e,i}) \, \rho_{e,i} + \sum_j H(\phi_{r,j}) \, \rho_{r,j} + \left(1 - \sum_i H(\phi_{e,i}) - \sum_j H(\phi_{r,j})\right) \rho_f \tag{20}$$

where $\rho_{e,i}$ and $\rho_{r,j}$ represent the density of the ith elastic body and the jth rigid body, respectively. Finally we note that the above formulation implicitly satisfies the boundary conditions at the interface (Eq. 3), and allows for the convenient use of common operators on the same solution space, across all the phases.

3.7. Body and contact forces

Effects of external bulk forcing such as gravity can be directly captured through an additional body force term $\boldsymbol{b} = \boldsymbol{g}$, where $\boldsymbol{g}$ is the acceleration due to gravity. Additionally, in certain situations, bodies might approach each other closely. In such cases we add to $\boldsymbol{b}$ an extra contact forcing term that pushes these objects apart, to prevent their interpenetration. Accordingly, we adopt the level set based contact forcing model described in Valkov et al. [25]

$$
\boldsymbol{b}_{\text{coll},i,j} = \begin{cases} k_{\text{coll}} \delta \left(\dfrac{\phi_i - \phi_j}{2} \right) \boldsymbol{n}_{i,j} & \phi_i < 0 \\ 0 & \text{otherwise} \end{cases}
\tag{21}
$$

Here k_{coll} is a constant while ϕ_i and ϕ_j correspond to the level sets capturing the interface of the two bodies. The symbol $\delta(\cdot)$ stands for the Dirac Delta function while $\boldsymbol{n}_{i,j}$ is a unit vector normal to the level sets of $\phi_i - \phi_j$ and pointing away from the midplane level set contour, where $\phi_i = \phi_j$.

3.8. Form of the Cauchy momentum equation to be numerically implemented

Here, we finally present the form of the Cauchy momentum equation that is ultimately discretized and numerically implemented. Taking the curl of Eq. 16, we obtain the vorticity formulation

$$
\frac{\partial \omega}{\partial t} + (\boldsymbol{v} \cdot \nabla) \omega = (\omega \cdot \nabla) \boldsymbol{v} - \frac{\nabla \rho}{\rho^2} \times \nabla p + \frac{1}{\rho} \nabla \times \nabla \cdot \boldsymbol{\sigma}' + \nabla \times \boldsymbol{b} + \nabla \times \lambda \sum_j H(\phi_{r,j})(\boldsymbol{v}_{r,j} - \boldsymbol{v}).
\tag{22}
$$

We then expand the baroclinic term as a function of the velocity [57] and, considering the fact that the stretching term $(\omega \cdot \nabla) \boldsymbol{v}$ vanishes in two dimensions, we rewrite this equation as

$$
\begin{aligned}
\frac{\partial \omega}{\partial t} + (\boldsymbol{v} \cdot \nabla) \omega = {} & -\frac{\nabla \rho}{\rho} \times \left(\frac{\partial \boldsymbol{v}}{\partial t} + \nabla \cdot (\boldsymbol{v} \otimes \boldsymbol{v}) - \boldsymbol{b} \right) \\
& + \frac{1}{\rho} \nabla \times \nabla \cdot \boldsymbol{\sigma}' + \nabla \times \boldsymbol{b} + \nabla \times \lambda \sum_j H(\phi_{r,j})(\boldsymbol{v}_{r,j} - \boldsymbol{v}).
\end{aligned}
\tag{23}
$$

With pressure p eliminated from the governing equations, an incompressible velocity field is then directly recovered from the vorticity by solving a Poisson equation using appropriate boundary conditions on Σ

$$
\nabla^2 \psi = -\omega; \quad \boldsymbol{v} = \nabla \times \psi
\tag{24}
$$

where $\psi : \Sigma \times \mathbb{R}^+ \mapsto \mathbb{R}$ corresponds to the streamfunction. In the next section, we proceed to describe the numerical discretization of the elements described above, with a detailed step by step explanation of the algorithm.

4. Numerical discretization and algorithm

We proceed to spatially discretize the system of equations (Eqs. 23 and 24) by adopting a Cartesian grid of uniform spacing h which forms our computational domain Σ_h. All fields defined earlier are replaced by their discrete counterparts, now defined on this discrete domain Σ_h. The temporal discretization is achieved via a Godunov split of Eq. 23, which leads to the algorithmic steps detailed in Algorithm 1. This splitting enables us to evaluate each step independently, providing the flexibility to conveniently mix explicit and implicit time integration (Eq. 31 and Eqs. 39 to 45), at the penalty of reducing convergence in time between first and second order (Section 5, [58]). In the following, we describe one full time step of the proposed algorithm, from t^n to t^{n+1}, assuming that all necessary quantities are known up to t^n.

4.1. Poisson solve and velocity recovery

We solve the Poisson Eq. 25 on the grid for periodic and unbounded boundary conditions ψ using a Fourier-series based $\mathcal{O}(n \log(n))$ solver. This allows us to exploit the diagonality of the Poisson operator in the case of periodic boundaries [89] to achieve spectral accuracy. For unbounded conditions, we use the zero padding technique of Hockney and Eastwood [89], while for mixed periodic–unbounded boundaries we use the approach of Chatelain and Koumoutsakos [90]. Once ψ is obtained on the grid, we recover the velocity per Eq. 26, through the discrete second order centered finite difference curl operator. At the boundaries, we use one-sided second order finite differences for consistent velocity recovery.

Algorithm 1 General algorithm.

Poisson solve (Section 4.1) $\nabla^2 \psi^n = -\omega^n$ (25)

Velocity recovery (Section 4.1) $\boldsymbol{v}^n = \nabla \times \psi^n + \boldsymbol{V}_\infty^n$ (26)

Rigid body level set recovery (Section 4.2) $\phi_{r,j}^n = \phi_{r,j}(\boldsymbol{x}_{\mathrm{cmr},j}^n, \theta_{r,j}^n, t^n)$ (27)

Translational projection (Section 4.2) $\dot{\boldsymbol{x}}_{\mathrm{cmr},j}^n = \dfrac{1}{M_{r,j}} \displaystyle\int_\Sigma \rho_{r,j} H_\varepsilon(\phi_{r,j}^n) \boldsymbol{v}^n d\boldsymbol{x}$ (28)

Rotational projection (Section 4.2) $\dot{\boldsymbol{\theta}}_{r,j}^n = \dfrac{1}{J_{r,j}} \displaystyle\int_\Sigma \rho_{r,j} H_\varepsilon(\phi_{r,j}^n) \left[(\boldsymbol{x} - \boldsymbol{x}_{\mathrm{cmr},j}^n) \times \boldsymbol{v}^n \right] d\boldsymbol{x}$ (29)

Rigid body velocity recovery (Section 4.2) $\boldsymbol{v}_{r,j}^n = \dot{\boldsymbol{x}}_{\mathrm{cmr},j}^n + \dot{\boldsymbol{\theta}}_{r,j}^n \times (\boldsymbol{x} - \boldsymbol{x}_{\mathrm{cmr},j}^n)$ (30)

Velocity penalization (Section 4.2) $\boldsymbol{v}_\lambda^n = \dfrac{\boldsymbol{v}^n + \lambda \Delta t^n \sum_j H_\varepsilon(\phi_{r,j}) \boldsymbol{v}_{r,j}^n}{1 + \lambda \Delta t^n \sum_j H_\varepsilon(\phi_{r,j})}$ (31)

Vorticity penalization (Section 4.2) $\omega_\lambda^n = \omega^n + \nabla \times (\boldsymbol{v}_\lambda^n - \boldsymbol{v}^n)$ (32)

Inverse map advection (Section 4.3) $\dfrac{\partial \boldsymbol{\xi}^n}{\partial t} + \boldsymbol{v}_\lambda^n \cdot \nabla \boldsymbol{\xi}^n = 0$ (33)

Inverse map based level set recovery (Section 4.4) $\phi_{e,i}^n = \phi_{e,i}^0(\boldsymbol{\xi}^n)$ (34)

Level set reinitialization (Section 4.4) $|\nabla \phi_{e,i}^n| = 1$ (35)

Inverse map extrapolation (Section 4.5) $\boldsymbol{\xi}_{\Sigma,\,\mathrm{extrap}}^n \leftarrow \boldsymbol{\xi}_{\Omega_e}^n$ (36)

Monolithic stress computation (Section 4.6) $\boldsymbol{\sigma}'^n = \boldsymbol{\sigma}'(\boldsymbol{\sigma}_f'^n, \boldsymbol{\sigma}_e'^n)$ (37)

Monolithic density computation (Section 4.6) $\rho^n = \rho(\phi_{e,i}^n, \rho_{e,i}, \phi_{r,j}^n, \rho_{r,j}, \rho_f)$ (38)

Stress based vorticity update (Section 4.6) $\dfrac{\partial \omega_\lambda^n}{\partial t} = \dfrac{1}{\rho^n} \left(\nabla \times \nabla \cdot \boldsymbol{\sigma}'^{,n} \right)$ (39)

Baroclinic term based vorticity update (Section 4.7) $\dfrac{\partial \omega_\lambda^n}{\partial t} = -\dfrac{\nabla \rho^n}{\rho^n} \times \left(\dfrac{\partial \boldsymbol{v}_\lambda^n}{\partial t} + \nabla \cdot (\boldsymbol{v}_\lambda^n \otimes \boldsymbol{v}_\lambda^n) - \boldsymbol{b}^n \right)$ (40)

Volumetric force term based vorticity update (Section 4.7) $\dfrac{\partial \omega_\lambda^n}{\partial t} = \nabla \times \boldsymbol{b}^n$ (41)

Vorticity advection and remeshing (Section 4.8) $\dfrac{\partial \omega_\lambda^n}{\partial t} + (\boldsymbol{v}_\lambda^n \cdot \nabla) \omega_\lambda^n = 0$ (42)

Vorticity propagation to next time step (Section 4.8) $\omega^{n+1} = \omega_\lambda^{n+1}$ (43)

Rigid body translational update (Section 4.9) $\boldsymbol{x}_{\mathrm{cmr},j}^{n+1} = \boldsymbol{x}_{\mathrm{cmr},j}^n + \dot{\boldsymbol{x}}_{\mathrm{cmr},j}^n \Delta t^n$ (44)

Rigid body rotational update (Section 4.9) $\theta_{r,j}^{n+1} = \theta_{r,j}^n + \dot{\boldsymbol{\theta}}_{r,j}^n \Delta t^n$ (45)

4.2. Projection and Brinkman penalization of rigid body motion

For each rigid body j in the simulation, we recover its level set per Eq. 27, followed by projection of translational $\dot{\boldsymbol{x}}_{\mathrm{cmr},j}^n$ (Eq. 28) and rotational $\dot{\boldsymbol{\theta}}_{r,j}^n$ (Eq. 29) velocities. The volume integrals are carried out using the mid-point rule with a discrete, mollified Heaviside integrand H_ε defined as

$$H_\varepsilon(q) = \begin{cases} 0 & q > \varepsilon \\ \dfrac{1}{2}\left[1 - \dfrac{q}{\varepsilon} - \dfrac{1}{\pi} \sin\left(\pi \dfrac{q}{\varepsilon}\right) \right] & |q| \leq \varepsilon \\ 1 & q < -\varepsilon \end{cases} \qquad (46)$$

where the mollification length $\varepsilon = 2\sqrt{2}h$ is set throughout the paper, h being the grid spacing. Rigid components of motion $\dot{\boldsymbol{x}}_{\mathrm{cmr},j}^n$ and $\dot{\boldsymbol{\theta}}_{r,j}^n$ so obtained are then employed to determine the rigid velocity fields $\boldsymbol{v}_{r,j}$, which are fed to the penalization operator (Eq. 31), to finally recover the physically consistent flow field $\boldsymbol{v}_\lambda^n$. The penalization operator for the velocity field is formulated through a first order implicit Euler time discretization scheme [58], to relax stability conditions related to the stiffness of the penalization parameter $\lambda = 10^4$ (throughout the paper). The additional vorticity caused by penalization $\nabla \times (\boldsymbol{v}_\lambda^n - \boldsymbol{v}^n)$ is added to the unpenalized vorticity ω^n via Eq. 32. This approach avoids additional diffusion of the ω field as reported in Rasmussen et al. [91]. For recent advances on Brinkmann penalization techniques, the reader is referred to [92–94].

4.3. Inverse map advection

After computing translational and rotational rigid body velocities and penalizing the flow field accordingly, we consider the elastic bodies present in the domain. We start by advecting the inverse map through Eq. 33. We do so by discretizing $\nabla \boldsymbol{\xi}$ using a WENO5 stencil [95] and performing the temporal integration using a SSP (Strong Stability Preserving) third order Runge-Kutta scheme [96]. The rationale behind this choice, as opposed to the use of particles and remeshing, stems from two observations. First, particle advection and moment conserving remeshing solve the conservative form of the advection equation, which, relative to Eq. 33, includes the additional term $\boldsymbol{\xi} \ (\nabla \cdot \boldsymbol{v})$ (see Appendix B). Although this extra term is zero for incompressible solids and fluids, its numerical discretization at the solid–fluid interface leads to small, localized and bounded non-zero values, due to the blending of the two phases (the term $\boldsymbol{\xi} \ (\nabla \cdot \boldsymbol{v})$ is instead, as expected, found to be zero in the bulk of both fluid and solid phases). These numerical errors are observed to cause high wave number instabilities in some cases (see Appendix B, Appendix C for further details). While modifications to the conservative form have been suggested to mitigate the issue [18], these cannot be directly translated to particle methods. Second, as observed in Hieber and Koumoutsakos [97], the advection of solid deformation maps through particles does not translate in the larger-time steps typically associated with particles' relaxed stability properties. Indeed, constraints due to solid shear wave speeds generally dominate (details on such time-step restrictions can be found in Section 4.10). Thus, the use of particles provide little incentive over a grid based non-oscillatory advection scheme. Hence, our choice of WENO5 in combination with SSP-RK3. We also note that the advection of the inverse map $\boldsymbol{\xi}$ (Eq. 33), unlike the advection of all other quantities (Eqs. 42, 44 and 45), is executed early on before the evaluation of Cauchy stress terms (Eq. 39) and baroclinic terms (Eq. 40). This is because of the fundamental difference in the formulation of flow–structure interaction in our algorithm, for rigid vs. elastic bodies. For rigid bodies, we purposefully advect all relevant quantities based on the previous time step's velocity field, to leverage the mismatch in interface position for the recovery, through projection, of the fluid forces acting upon the body. On the other hand, the elastic body–fluid interaction necessitates the evaluation of explicit forces and torques at the latest solid configuration (Eq. 37), which can only be computed by first advecting the inverse map $\boldsymbol{\xi}$ using Eq. 33, to obtain the solid configuration at the current time step.

4.4. Level set recovery and reinitialization

Using the advected inverse map we can reconstruct the deformed solid interface at the next time step using Eq. 34. However discretization errors corrupt this reconstructed level set field [23] prompting the need to reinitialize it to restore the signed-distance property of Eq. 35. Here we utilize the second order accurate variant of the fast marching method (FMM) described in [23] to reinitialize $\phi_{e,i}$, in a narrow band of 8 points on either side of the solid zone.

4.5. Inverse map extrapolation

As specified in Section 3.5, $\boldsymbol{\xi}$ is only defined inside the solid phase Ω_e. However, to numerically evaluate and eventually merge stresses between solid and fluid, it is necessary to *extend* $\boldsymbol{\xi}$ into the nearby fluid zone. This step, indicated in Eq. 36, is achieved by using the least-squares based extrapolation procedure reported by Jain et al. [18]. In this work, we extrapolate information across 6 grid points, compatibly with the stencil support of the spatial operators that will act on it.

4.6. Stress evaluation and vorticity update

Here, we elaborate on the numerics involved in Eqs. 37 to 39. First, the deformation gradient tensor $\boldsymbol{F}$ and the strain rate tensor $\boldsymbol{D}'$ are computed by taking derivatives of $\boldsymbol{\xi}$ and $\boldsymbol{v}$ respectively, using second order centered finite differences. Following the computation of $\boldsymbol{F}$ and $\boldsymbol{D}'$, we then compute the solid and fluid stresses $\boldsymbol{\sigma}'_e$ and $\boldsymbol{\sigma}'_f$, using the solid and fluid constitutive laws given in Eqs. 5, 6 and 11. The mollified Heaviside function Eq. 46 is then used to blend the solid and fluid stresses (Eq. 19) and density (Eq. 20) to obtain monolithic stress and density fields. We then compute the Cauchy stress contribution shown in Eq. 39 in two steps. In the first step, we compute $\nabla \cdot \boldsymbol{\sigma}'$ by taking derivatives of $\boldsymbol{\sigma}'$ using second order centered finite differences. In the second step, we compute $\nabla \times (\nabla \cdot \boldsymbol{\sigma}')$ by replacing the curl operator $\nabla \times$ with its discrete second order centered finite difference counterpart. The Cauchy stress contribution is then added to the vorticity in a forward Euler step. With regards to this last step, we recommend, as already noted in Section 4.3, that the solid stress should be evaluated after the inverse map advection step Eq. 33. We have observed this ordering to be robust and numerically stable.

Finally, we bring attention to the specific domain of viscosity dominated problems, where the bodies and the fluid have the same density ($\rho_{e,i} = \rho_{r,j} = \rho_f = \rho$) and the same dynamic viscosity ($\mu_{e,i} = \mu_f = \mu$). In this case, Eq. 39 simplifies to the following equation

$$\frac{\partial \omega_\lambda^n}{\partial t} = \frac{1}{\rho} \left(\nabla \times \nabla \cdot \sum_i H(\phi_{e,i}^n) \, \boldsymbol{\sigma}'^n_{e,i} \right) + \frac{\mu}{\rho} \nabla^2 \omega_\lambda^n. \tag{47}$$

As a consequence, in the case of a periodic domain, the diagonality of the ∇^2 operator in the Fourier space (RHS of Eq. 47) can be leveraged to achieve unconditionally stable temporal integration of the viscous stress contribution to the vorticity field, as detailed in Kolomenskiy and Schneider [98]. Hence, the Fourier condition (Section 4.10) for the explicit update of viscous stresses can be sidestepped to achieve faster time-to-solutions.

4.7. Baroclinic and volumetric force terms

We compute the baroclinic contribution of Eq. 40 as in Gazzola et al. [58], where the baroclinic term itself (RHS) is recovered directly from the linear momentum balance of the Navier–Stokes equations. This treatment is introduced to bypass the expensive computation of the pressure field. We use discrete second order centered finite differences for the gradient operator ∇, while the temporal derivative is approximated to first order using the differences $\boldsymbol{v}_\lambda^n - \boldsymbol{v}_\lambda^{n-1}$. The baroclinic contribution is then added to the vorticity in a forward Euler step. This treatment of the baroclinic term has been empirically shown [58,62] to be accurate for low density contrasts. Nonetheless, we note that no rigorous convergence proof is available, and that for higher density ratios computation of the pressure field may become necessary [65] to ensure accuracy.

We then further evolve the vorticity generated from the volumetric forcing terms in Eq. 41, again through a forward Euler step. Lastly, in the case of a collision between two bodies, Eq. 21 is used to compute collision forces, substituting the Dirac Delta function with its mollified equivalent δ_ε, as defined below.

$$\delta_\varepsilon(q) = \begin{cases} 0 & q > \varepsilon \\ -\dfrac{1 + \cos\left(\pi\frac{q}{\varepsilon}\right)}{2\varepsilon} & |q| \leq \varepsilon \\ 0 & q < -\varepsilon \end{cases}$$

4.8. Vorticity advection and remeshing

After updating the vorticity on the grid, we discretize it into particles of strength

$$\Gamma_p = \sum_i \omega_i W\left(\frac{\boldsymbol{x}_i - \boldsymbol{x}_p}{h}\right)$$

where i symbolizes the grid index, p is the particle and $W(\cdot)$ is an interpolation kernel. In this work we used the second order M_4' with $W(\boldsymbol{x}) = M_4'(x)M_4'(y)$ which conserves the first three moments [99]. Regarding our choice of a M_4' kernel, we were motivated by its minimal artificial diffusion (during remeshing), implementation simplicity and accuracy consistent with the second-order spatial discretization of all differential operators. We noticed empirically that the absence of sign-preservation in the M_4' kernel when advecting vorticity was not an issue [100], similar to our previous studies [58]. Following interpolation, these particles are then advected using a third order Runge-Kutta scheme. The vorticity carried by the particles is then remeshed at the grid nodes via the same interpolation kernel and carried forth to the next time step (Eq. 43).

4.9. Rigid body update

Finally we evolve the position and orientation of all rigid bodies in the simulation using the first order explicit Euler time integration scheme for reasons detailed in Gazzola et al. [58].

4.10. Restrictions on simulation time step

We encounter four major time step restrictions in our algorithm due to the presence of different time scales in the coupling problem. The first restriction is associated with particle advection and remeshing (Eq. 42). This restriction is not dictated by the usual CFL (Courant–Friedrich–Lewy) condition. Instead Δt is constrained by the amount of extension and shear through the Lagrangian LCFL condition, which is independent of grid spacing h

$$\Delta t_1 \leq \text{LCFL } \max(||\omega||_\infty, ||\nabla \boldsymbol{v}||_\infty)^{-1}. \tag{48}$$

Physically, this condition necessitates that particle remeshing kernels should always overlap in space at all times. The independence from h indicates that our particles based approach can take larger-than-CFL stable time steps, reducing time-to-solution. A second restriction stems from the need to resolve shear waves inside elastic solids. This is a CFL-like restriction dependent on the shear wave speed c_{sh}

$$\Delta t_2 \leq h \text{ CFL } c_{sh}^{-1} = h \text{ CFL } \sqrt{\rho_e/G}. \tag{49}$$

Here, ρ_e and G correspond to the solid density and shear modulus, respectively. Another related restriction stems from the advection of the inverse map $\boldsymbol{\xi}$ inside the elastic solid

$$\Delta t_3 \leq h \, \text{CFL} \, ||\boldsymbol{v}_e||_\infty^{-1} \tag{50}$$

where $\boldsymbol{v}_e$ refers to the velocity field inside the elastic solid. We note that the above Eqs. 49 and 50 also capture constraints relative to the elastic stress-based vorticity update of Eq. 39. This is because elastic stresses propagate as waves inside the solid with same speed $\boldsymbol{v}_e$ which in turn is limited by $c_{sh} = \sqrt{G/\rho_e}$, thus no additional stability condition is necessary for Eq. 39. We observe that in most cases $\Delta t_3 > \Delta t_2$, rendering the condition on shear waves more stringent. Finally, the fourth restriction is the Fourier condition that ensures stability with regards to explicit time discretization of the viscous stresses inside both the solid and fluid

$$\Delta t_4 \leq k \, (h)^2 / 4 \max(\nu_f, \nu_e) \tag{51}$$

where k is a constant usually set to be ≤ 1. Here we set $k = 0.9$ throughout. We note that in purely periodic domains with uniform viscosity, we can utilize an implicit discretization of the viscous terms (Section 4.6), effectively side-stepping this restriction. Combining Eqs. 48 to 51, we obtain the final criterion to adapt the time step during simulation

$$\Delta t = \min[\Delta t_1, \Delta t_2, \Delta t_3, \Delta t_4]. \tag{52}$$

We observe (a posteriori) that in several cases investigated in Section 5 and Section 6, the time-step restriction from the high elastic shear wave speeds Δt_2, rather than the LCFL condition Δt_1, limits the global time-step Δt. This mismatch in time scales does not allow us to take full advantage of particle advection and associated relaxed stability properties (LCFL). Potential solutions to improve computational efficiency consist in the use of local time stepping techniques [61] or implicit update of solid stresses [101]. Nonetheless, we wish to point out that for flow advection dominated regimes where Δt_1 restricts the global time-step, our approach does benefit from relaxed stability properties of vortex methods (LCFL) to achieve faster time-to-solutions. Such regimes are relevant and broadly encountered in biology and engineering, from vascular flows [102] to energy-harvesting [62] applications. A demonstration is presented here through the flapping flag example of Section 6.3.

Following a detailed description of our algorithm, we now investigate the accuracy and convergence properties of our algorithm, via extensive validation across analytical and numerical benchmarks.

5. Validation benchmarks

We now proceed to validate the proposed method across several benchmark cases. These involve a pure solid system, forced oscillations in parallel layers of fluid and solid, fluid induced shape oscillations of a visco-hyperelastic cylinder, and collision between two hyperelastic cylinders surrounded by fluid. For all these cases, the dimensional parameters are specified in SI units, unless otherwise noted. Additionally, they all utilize a square computational domain of unit dimension $[0, 1]^2$. For each case, we conduct a convergence analysis by reporting discrete L_2 and L_∞ error norms of relevant physical quantities as a function of spatial and temporal discretization. We use the following definition of discrete norms

$$L_2(e) := \|e\|_2 = \sqrt{h^2 \sum_i |e_i|^2}; \quad L_\infty(e) := \|e\|_\infty = \max_i |e_i|; \quad e := p - p_{\text{ref}} \tag{53}$$

where e denotes the error, p is a physical quantity obtained from our method, p_{ref} is the reference solution, h denotes grid spacing and i denotes the grid point index, unless otherwise noted.

Depending on the specific problem, the dynamics at play may be governed by one or more key dimensionless numbers. We list them here, together with their physical interpretation

$$Re := \frac{\rho_f V L}{\mu_f} \sim \frac{\text{inertial forces}}{\text{viscous forces}}; \quad Cau := \frac{\rho_e V^2}{G} \sim \frac{\text{inertial forces}}{\text{elastic forces}}; \quad Er := \frac{\mu_f V}{GL} \sim \frac{\text{viscous forces}}{\text{elastic forces}} \tag{54}$$

where Re, Cau, Er, V, L, μ_f, ρ_f, ρ_e and G correspond to the Reynolds number, Cauchy number [103], Ericksen number [104], velocity scale, length scale, fluid viscosity, fluid density, elastic solid density and shear modulus of the solid, respectively.

5.1. Pure solid system

We first test our method for the case of a pure solid system, previously reported by Zhao et al. [42]. This case utilizes the components of the algorithm only pertaining to the solid phase—Poisson solve, solid stress update, diffusion and advection—the other components will be analyzed in the subsequent benchmarks. The neo-Hookean solid, shown in Fig. 2a, is initialized to be stress free and entails periodic boundaries. Following the method of manufactured solutions [105], we first derive a
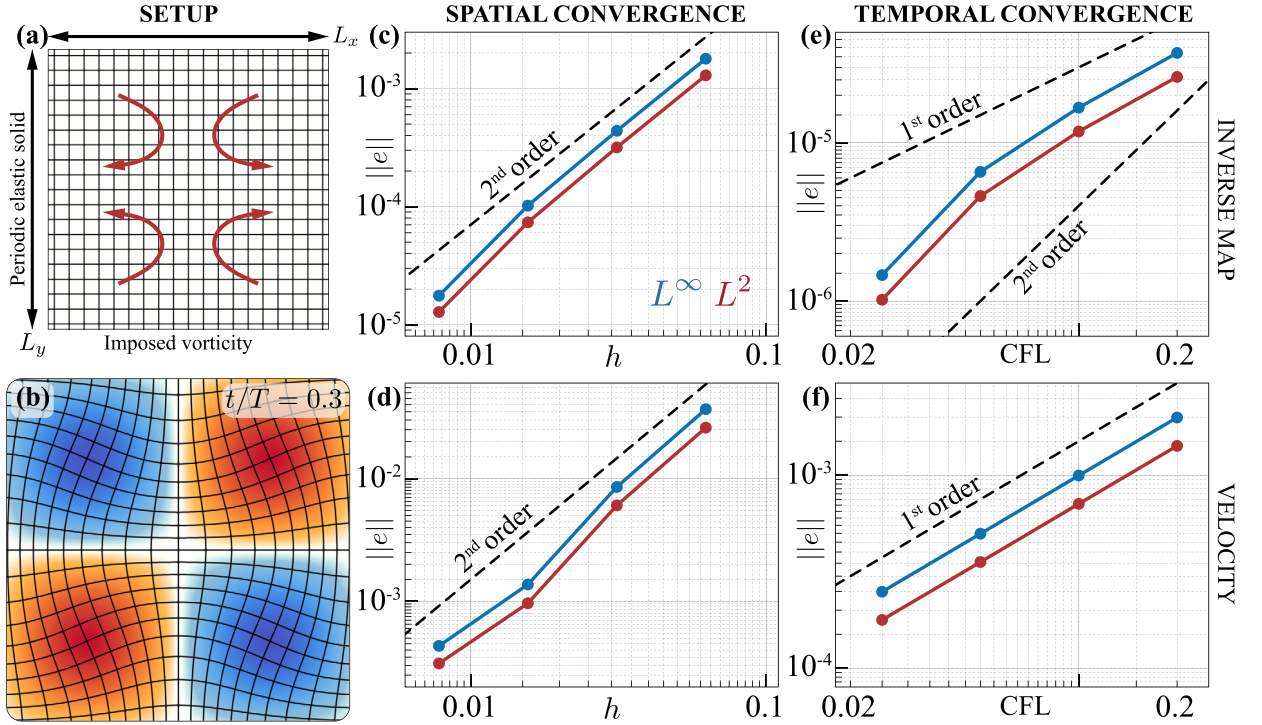
Fig. 2. Pure solid system. (*a*) Case setup. The neo-Hookean solid used is purely hyperelastic ($\mu_e = 0$), has $\rho_e = 1$ and has shear modulus $c_1 = 0.5$ i.e. $G = 2c_1 = 1.0$. The parameters for the imposed vorticity are $\omega_0 = 0.05$, $T = 1$ and $L_x = L_y = L = 1$. The key non-dimensional parameter for this benchmark is $Cau = \rho_e \omega_0^2 L^2 / G = 5 \times 10^{-4}$. (*b*) Deformed solid system with inverse map (black lines) and imposed vorticity field (orange/blue represent positive/negative vorticity) contours at $t/T = 0.3$. Spatial convergence: L_∞ (blue) and L_2 (red) norms of the error are plotted against grid spacing h, for (*c*) inverse map and (*d*) velocity, respectively. Temporal convergence: L_∞ (blue) and L_2 (red) norms of the error are plotted against CFL, for (*e*) inverse map and (*f*) velocity, respectively.

semi-analytical reference solution against which we validate our solver. We start by computing the semi-analytical inverse map $\boldsymbol{\xi}_{\text{sa}}$ resulting from the advection of $\boldsymbol{\xi}^0 = (X, Y)$ through the imposed velocity field

$$\boldsymbol{v}_{\text{ref, x}}(t) = \frac{L_x^2 L_y}{2\pi (L_x^2 + L_y^2)} \omega_0 \sin(2\pi t/T) \sin(2\pi x/L_x) \cos(2\pi y/L_y)$$

$$\boldsymbol{v}_{\text{ref, y}}(t) = \frac{-L_x L_y^2}{2\pi (L_x^2 + L_y^2)} \omega_0 \sin(2\pi t/T) \cos(2\pi x/L_x) \sin(2\pi y/L_y)$$

(55)

which corresponds to the vorticity field

$$\omega_{\text{ref}}(t) = \omega_0 \sin(2\pi t/T) \sin(2\pi x/L_x) \sin(2\pi y/L_y)$$

(56)

where ω_0 is a constant, L_x and L_y are the dimensions of the computational domain, and T is the time period of the imposed motion. Details relative to these quantities and the computational setup can be found in the caption of Fig. 2. We then calculate the external body force $\boldsymbol{b}_{\text{ext}}(\boldsymbol{x}, t)$ that needs to be applied to the solid at rest $\boldsymbol{\xi}^0$ to reproduce the above motion

$$\boldsymbol{b}_{\text{ext}} = \frac{\partial \omega_{\text{ref}}}{\partial t} + \boldsymbol{v}_{\text{ref}} \cdot \nabla \omega_{\text{ref}} - \nabla \cdot \boldsymbol{\tau}_{\text{elas}}\left(\boldsymbol{\xi}_{\text{sa}}\right)$$

(57)

where the dependence of solid stress $\boldsymbol{\tau}_{\text{elas}}$ on the previously computed inverse map $\boldsymbol{\xi}_{\text{sa}}$ is made explicit. All operators are either analytical or discretized as in Section 4. We then perform a separate simulation using our numerical method, in which we apply this force $\boldsymbol{b}_{\text{ext}}(\boldsymbol{x}, t)$ to the solid at rest and record the output numerical velocity $\boldsymbol{v}$ and inverse map $\boldsymbol{\xi}$ at a prescribed point of time. The convergence order for both the inverse map $\boldsymbol{\xi}$ and velocity field $\boldsymbol{v}$ is finally determined by computing the L_2 and L_∞ norms (Eq. 53) relative to the semi-analytical inverse map $\boldsymbol{\xi}_{\text{sa}}$ (at the finest resolution 512×512, CFL, LCFL $= 0.1$) and the analytical velocity field $\boldsymbol{v}_{\text{ref}}$. For spatial convergence, we fix Δt based on CFL = LCFL = 0.05 at grid resolution 128×128, and vary the spatial resolution between 16×16 and 128×128. For temporal convergence instead, we set the spatial resolution to 256×256 and vary the CFL = LCFL between 0.025 and 0.2. As seen in Fig. 2c,d the method presents second order spatial convergence for both the inverse map and velocity field, which is in agreement with our

spatial discretization of the operators. Temporal convergence (Fig. 2e,f) is instead found to be between first and second order (least squares fit of 1.5) for the inverse map and first order for the velocity field, as expected from the Godunov splitting adopted in the timestepping algorithm (Eqs. 39 to 42).

5.2. Oscillatory response in parallel layers of fluid and solid

Having tested the ability of our method to capture purely elastic responses of the solid media, we now proceed to validate the interfacial coupling between solid and fluid phases. We adopt the benchmark setup shown in Fig. 3a, first proposed by Sugiyama et al. [26]. Here an elastic solid layer is sandwiched between two fluid layers, in turn confined by two long planar walls, whose horizontal oscillations drive a characteristic system response. Indeed, this setting admits a time periodic, one-dimensional analytical solution, which we generalized from Sugiyama et al. [26] to include visco-hyperelastic, density mismatched solid [106]. Overall, this problem entails multiple interfaces, phases and boundary conditions interacting dynamically, and serves as a challenging benchmark to validate the long time behavior, stability and accuracy of our solver.

We computationally realize this setup as shown in Fig. 3b. Instead of modeling the walls as a kinematic condition at the boundaries of the fluid phase, we actually represent the walls within the computational domain as Brinkman solids. This choice enables us to test rigid solid, elastic solid and fluid coupling in the same simulation while demonstrating the flexibility of our method. Then, periodic and unbounded boundary conditions are imposed in the x and y directions respectively [90]. We investigate two separate cases in which the density matched visco-elastic solid is either made of a neo-Hookean material or a generalized Mooney-Rivlin material [71]. The system starts from rest in a stress free state and the simulation is run well beyond the initial transient phase, resulting in periodic dynamics. Details can be found in the figure caption.

Fig. 3c showcases the numerical x velocity field and the inverse map contours at the time of maximal deformation $(t/T = 0.75)$ for the neo-Hookean case. We plot the corresponding non-dimensional x velocities at the marked line station for $t/T = 0.75$ and $t/T = 1$ in Fig. 3d, onto which the analytical solution is overlaid. As it can be seen our simulations compare well with the benchmark, with the maximum deviation occurring at the solid–fluid interface. This is expected given that our approach involves a diffuse interface. We then plot the L_2 and L_∞ norms of the error e defined as $e = (\boldsymbol{v}_{\text{sim}} - \boldsymbol{v}_{\text{analytical}}) \cdot \hat{i}$ at different time instances, for spatial resolutions between 32×32 and 512×512 (Fig. 3e). The L_2 convergence is approximately second order ($L_2 = 1.8$), while for L_∞ it is closer to first order ($L_\infty = 1.3$). This is because of the localized errors at the interface, where a C^1 discontinuity of the physical solution is observed.

Fig. 3f-h refer to the generalized Mooney–Rivlin case. The effect of solid non-linearity can be seen from the inverse map contours (Fig. 3f) and corresponding velocities within the solid phase in Fig. 3g, and manifest as a sharp "bend" in the solid midplane at $y/(L_f + L_s) = 0.25$. Once again, numerical and analytical results are in agreement. Convergence of errors with spatial resolution (Fig. 3h) shows trends similar to the case with the neo-Hookean constitutive model (1.5 for L_2 and 0.9 for L_∞).

The results of this section indicate the ability of our approach to successfully capture fluid–elastic solid and fluid–rigid solid interactions that are themselves coupled. This ability extends to setups involving baroclinic effects arising from mismatched densities in the elastic solid. We showcase this for a case with $\rho_e = 2$, $\rho_f = 1$ in Appendix A and observe consistent convergence and accuracy properties.

5.3. Fluid induced shape oscillations of a visco-hyperelastic cylinder

We now test the capability of capturing dynamics related to time dependent geometrical variations of a two-dimensional fluid–solid interface. To do so we adopt the benchmark setup of a neutrally buoyant freely oscillating cylinder immersed in a fluid, first reported by Zhao et al. [42]. Fig. 4a highlights the initial physical setup—a stress free cylinder surrounded by fluid is placed at the center of the domain with periodic boundaries. We then deform the solid through an initial imposed Taylor–Green vorticity field, corresponding to the streamfunction profile

$$\psi = \psi_0 \sin(2\pi x/L_x) \sin(2\pi y/L_y) \tag{58}$$

where ψ_0 is a constant and L_x, L_y are the dimensions of the computational domain (details in Fig. 4).

Fig. 4b-d showcase the temporal evolution of inverse map, vorticity contours and the observed dynamics of the cylinder, which resembles a damped oscillator. Deformed initially by the imposed vorticity, the cylinder retracts due to its elastic response. This sets up oscillations, which slowly decay over time as the solid dissipates its elastic potential energy due to viscous effects. We then track the temporal variation of the kinetic energy of the system and strain energy of the solid, and compare with previous calculations based on finite elements [42,107] and finite volumes [18]. System kinetic energy KE and solid strain energy SE are defined and discretized as follows

$$\text{KE} = \int_\Sigma \frac{1}{2} |\boldsymbol{v}|^2 \, d\boldsymbol{x} \approx \frac{h^2}{2} \sum_i |\boldsymbol{v}_i|^2; \quad \text{SE} = \int_{\Omega_e} c_1 (tr(\boldsymbol{F}^T \boldsymbol{F}) - 2) \, d\boldsymbol{x} \approx c_1 h^2 \sum_i \text{sgn}(\phi_i)(tr(\boldsymbol{F}_i^T \boldsymbol{F}_i) - 2) \tag{59}$$
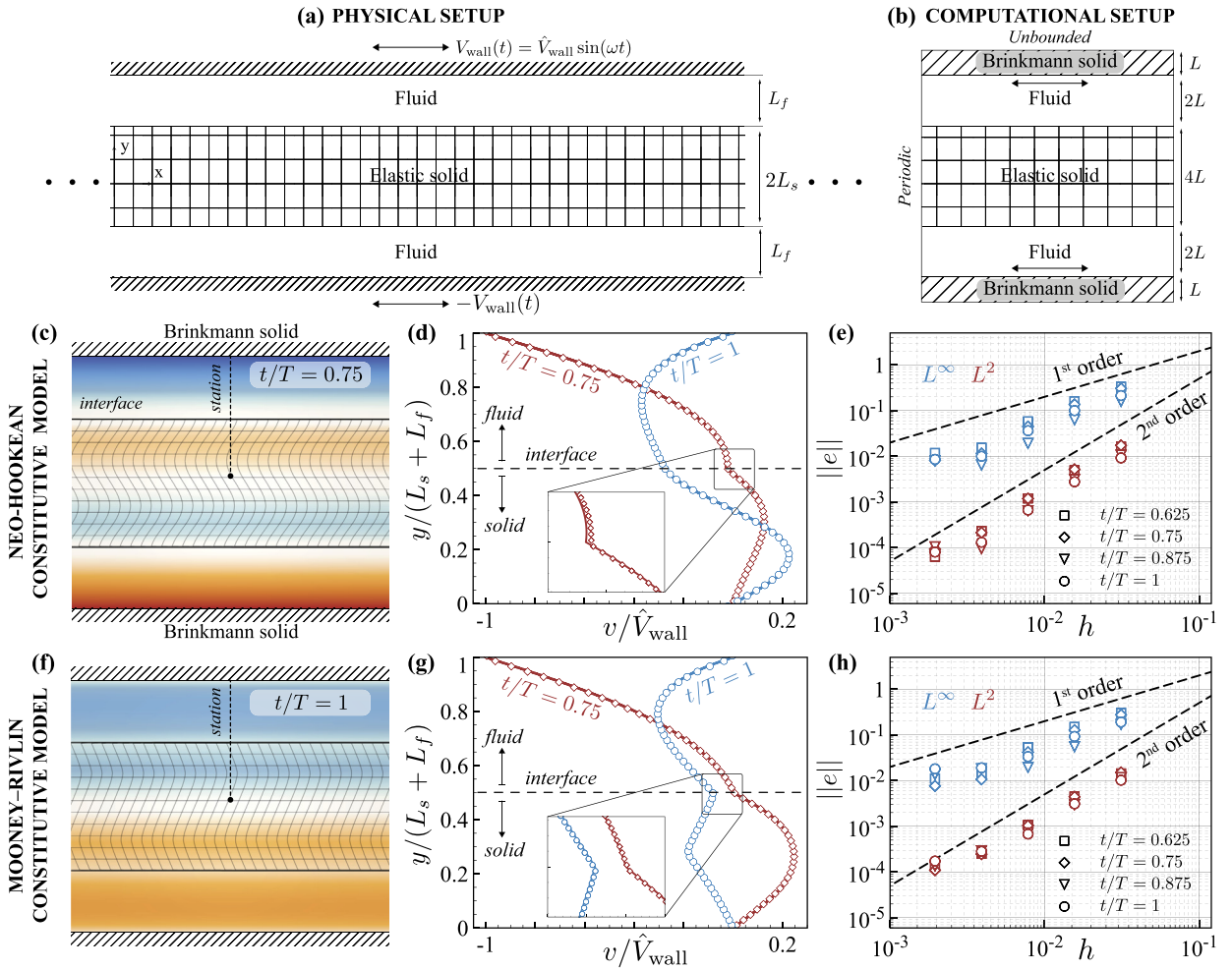
Fig. 3. Oscillatory response in parallel solid–fluid layers. (*a*) Physical setup of the parallel solid–fluid layers, with the walls moving sinusoidally in opposite directions with an imposed velocity $V_{\text{wall}}(t) := \pm \hat{V}_{\text{wall}} \sin(\omega t)$. (*b*) Computational setup indicating the boundary conditions and the use of a Brinkman solid to model the walls. Here, we set the thickness of the elastic slab to $2L_s = 4L$, each fluid layer to $L_f = 2L$ and each Brinkman solid layer to L, with $L = 0.1$. The system is hence symmetric about the mid-plane. The kinematic parameters used in the simulation are $\omega = \pi$, $T = 2\pi/\omega = 2$, $\hat{V}_{\text{wall}} = 0.4$, leading to a shear rate of $\dot{\gamma} = \hat{V}_{\text{wall}}/(L_s + L_f) = 1$. The dynamic parameters corresponding to the fluid phase are $\rho_f = 1$, $\mu_f = 0.02$. The neo-Hookean visco-elastic solid used in (*c-e*) is density matched ($\rho_f = \rho_e$), has dynamic viscosity $\mu_e = 0.1\mu_f$ and has shear modulus $c_1 = 0.01$ i.e. $G = 2c_1 = 0.02$. For the generalized Mooney–Rivlin material used in (*f-h*), we retain the parameters above and additionally set $c_2 = 0$, $c_3 = 4c_1$. The meanings of these coefficients are detailed in [71]. The simulations are run until $t/T = 10$, and physical quantities are sampled within the last cycle. The key non-dimensional dynamic parameters for this benchmark are $Re = \rho_f \dot{\gamma} L_f^2/\mu_f = 2$, $Er = \mu_f \hat{V}_{\text{wall}}/2GL_s = 1$. The computational parameters are set to LCFL = 0.05, CFL = 0.1. (*c, d, e*) Results for the solid with neo-Hookean constitutive law. (*c*) Velocity field (orange/blue represent positive/negative velocity) and inverse map contours within the domain, with the interface marked (black, thick solid) for visual clarity. Upon plotting the velocity profiles at the highlighted station (black, dashed) in the center of the domain, good agreement with analytical results is observed across all times as shown in (*d*), which plots the non-dimensional station position versus *x*-velocity. The inset shows the concentration of errors near the diffuse interface. For reference, numerical results are plotted with scatter points whereas analytical results are plotted with a solid line. Tracking these results with changing resolution results in the convergence plot shown in (*e*) where L_∞ (blue) and L_2 (red) norms of the error are plotted against grid spacing h at different t/T. Trends indicate a first to second order convergence as expected. (*f, g, h*) Results for the solid with generalized Mooney–Rivlin constitutive law are found to be consistent with the above trends.

As can be seen in Fig. 4e, our results show agreement with respect to the energy diagnostics (magnitudes, decay rate and phase lag) consistent with previous calculations obtained through a range of formulations, from mixed Eulerian-Lagrangian finite elements and finite differences [42] to completely Eulerian and based on finite volumes [18].

We then present spatial and temporal convergence of energies, inverse map $\boldsymbol{\xi}$ and velocity field $\boldsymbol{v}$ at $t = 0.25$, by computing the L_2 and L_∞ norms of the error field, with respect to the best resolved case. For spatial convergence, we fix Δt based on CFL = LCFL = 0.2 for the grid resolution 1024×1024, and vary the spatial resolution between 32×32 and 512×512 (with 1024×1024 as the best resolved case). For temporal convergence instead, we set the spatial resolution to 256×256 and vary the CFL = LCFL between 0.2 and 0.025 (with CFL = LCFL = 0.0125 as the best resolved case). As seen from Fig. 4f, the method presents spatial convergence between first and second order ($L_2 = L_\infty = 1.5$) for energies and inverse map. The convergence order for the velocity field was found to be first order for L_∞ and 1.4 for L_2. As shown in
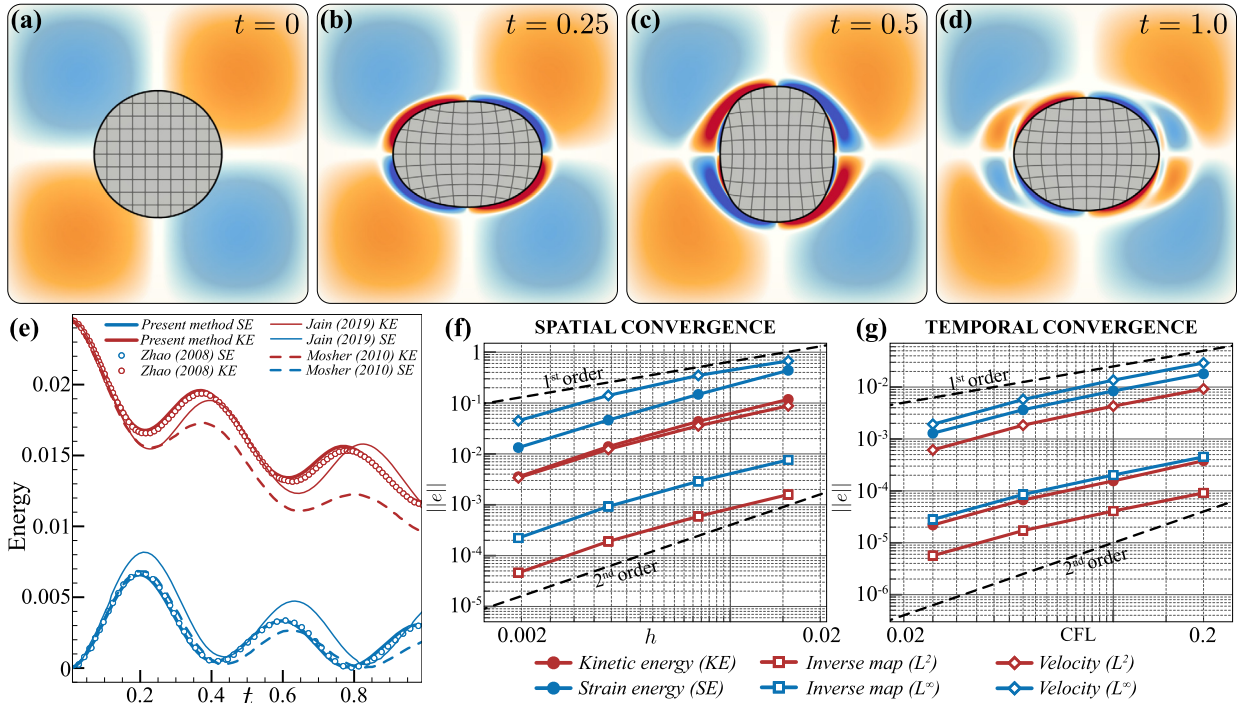
Fig. 4. Fluid induced shape oscillations of a visco-hyperelastic cylinder. (*a*) Case setup. The dynamic parameters corresponding to the fluid phase are $\rho_f = 1$, $\mu_f = 10^{-3}$. The neo-Hookean visco-hyperelastic cylinder, placed at (0.5, 0.5), has radius $r = 0.2$, is density matched ($\rho_s = \rho_f$), has dynamic viscosity $\mu_e = \mu_f$, and has shear modulus $c_1 = 0.5$ i.e. $G = 2c_1 = 1.0$. The parameters corresponding to the streamfunction for the imposed vorticity are $\psi_0 = 0.05$, and $L_x = L_y = L = 1$. The key non-dimensional parameters for this benchmark are $Re = \rho_f \psi_0 r / \mu_f L = 10$ and $Cau = \rho_e \psi_0^2 / GL^2 = 5 \times 10^{-4}$. (*b-d*) Temporal variation of inverse map (black lines) and vorticity field (orange/blue represent positive/negative vorticity) contours, showing the dynamic response of the cylinder to the initial imposed vorticity. (*e*) Comparison of temporal variation of the kinetic energy KE and strain energy SE with previous studies [18,42,107]. (*f*) Spatial convergence: L_∞ (blue) and L_2 (red) norms of the error are plotted against grid spacing h, for the energies, inverse map and velocity. (*g*) Temporal convergence: L_∞ (blue) and L_2 (red) norms of the error are plotted against CFL, for the energies, inverse map and velocity.

Fig. 4g, the temporal convergence order was found to be between first and second order ($L_2 = L_\infty = 1.3$), for all concerned quantities.

We note that this case is subject to an impulsive start, due to our initial condition in Eq. 58, which may pose additional numerical challenges. Our solver has been shown to robustly capture similar impulsive starts for rigid bodies [58] when compared against established, theoretical results [108]. Furthermore, the comparison with other numerical results at times $t < 0.1$ in Fig. 4 reveals good agreement. Both these observations are indicative of our solver's ability to resolve system dynamics that involve impulsive starts of rigid and elastic bodies. A further quantitative assessment, in the case of elastic bodies, would require a theoretical asymptotic analysis for small time instants around $t = 0$, which is beyond the scope of the current paper.

5.4. Collision between two hyperelastic cylinders immersed in a fluid

Following successful validation of our method for a single elastic body–fluid interaction, we now demonstrate the ability of our solver to capture interactions between multiple elastic bodies immersed in a fluid. Accordingly, we reproduce the case of collision between two hyperelastic neo-Hookean cylinders in a fluid, first reported by Jain et al. [18]. Additionally, this case also highlights the capability of our solver to simulate purely hyperelastic solids in a numerically stable fashion without the need for internal viscous dissipation μ_s. Fig. 5a presents the initial physical setup with two stress free neutrally buoyant circular cylinders immersed in a fluid, occupying a square domain with periodic boundaries. The system then evolves due to an initial imposed Taylor–Green vorticity field, corresponding to the streamfunction described in Eq. 58. Computational setup details can be found in Fig. 5.

Fig. 5b-d showcase the temporal dynamics of the two cylinders, along with the inverse map and vorticity contours. The imposed vorticity causes the two cylinders to collide, to then rebound due to both contact forces and the internal stresses generated as a result of the deformation. We validate our solver by comparing the temporal variation of the centroids of both cylinders, against previous results [18]. As seen in Fig. 5e, our results show close agreement with the benchmark [18].

We then present the spatial and temporal convergence of the inverse map $\boldsymbol{\xi}$ and velocity field $\boldsymbol{v}$ at $t = 0.3$, with respect to the best resolved case. For spatial convergence, we fix CFL = LCFL = 0.1 and vary the spatial resolution between 64×64 and 512×512 (with 1024×1024 as the best resolved case). For temporal convergence instead, we set the spatial resolution
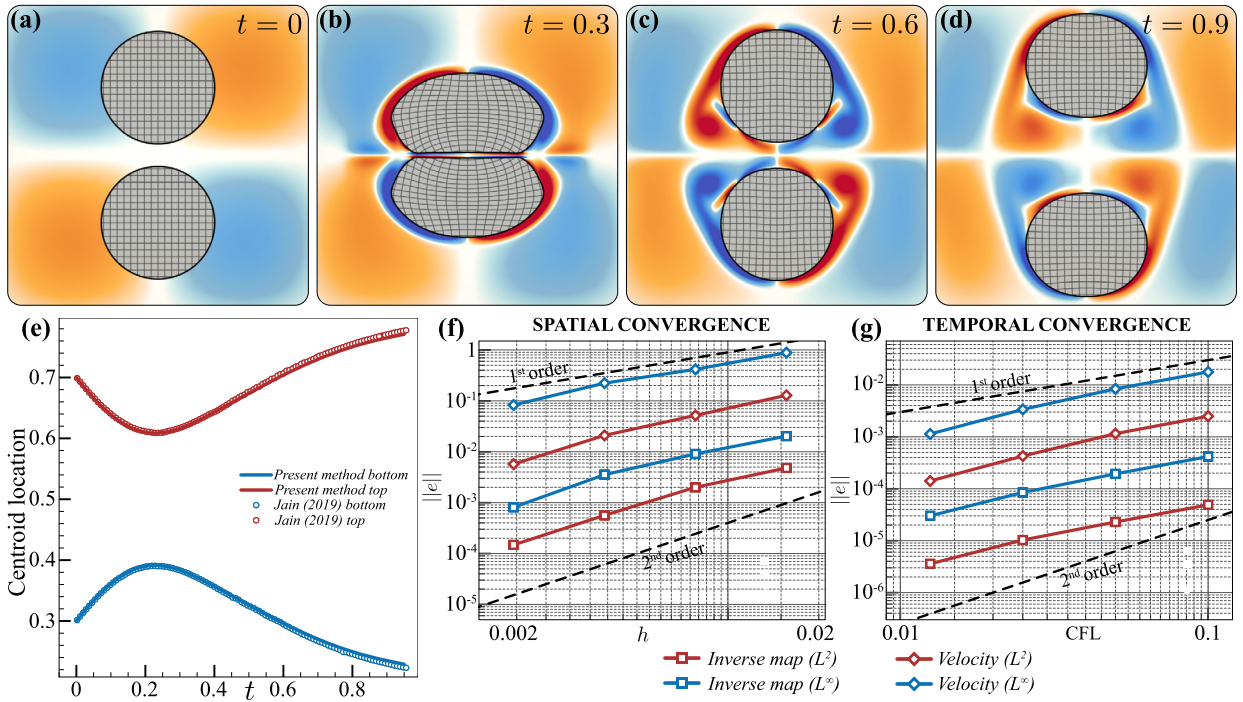
Fig. 5. Collision between two hyperelastic cylinders immersed in a fluid. (a) Case setup. The dynamic parameters corresponding to the fluid phase are $\rho_f = 1$, $\mu_f = 10^{-2}/2\pi$. The neo-Hookean hyperelastic disks, located at (0.5, 0.3) and (0.5, 0.7), have radii $r = 1/6$, are density matched ($\rho_e = \rho_f$), have no internal dissipation ($\mu_e = 0$), and have shear modulus $c_1 = 1.0$ i.e. $G = 2c_1 = 2.0$. The parameters corresponding to the streamfunction for the imposed vorticity are $\psi_0 = 1/2\pi$, and $L_x = L_y = L = 1$. The key non-dimensional parameters for this benchmark are $Re = \rho_f \psi_0 r/\mu_f L = 16.67$ and $Cau = \rho_e \psi_0^2 / GL^2 = 0.0127$. ($b$-$d$) Temporal variation of inverse map (black lines) and vorticity field (orange/blue represent positive/negative vorticity) contours, showing the dynamic response of the cylinders to the initial imposed vorticity. (e) Comparison of temporal variation of the centroids of the cylinders with previous studies [18]. (f) Spatial convergence: L_∞ (blue) and L_2 (red) norms of the error are plotted against grid spacing h, for the inverse map and velocity. (g) Temporal convergence: L_∞ (blue) and L_2 (red) norms of the error are plotted against CFL, for the inverse map and velocity.

to 256×256 and vary the CFL = LCFL between 0.1 and 0.0125 (with CFL = LCFL = 0.00625 as the best resolved case). As seen from Fig. 5f, the method presents spatial convergence between first and second order for inverse map (1.7 for L_2 and 1.5 for L_∞) and velocity field (1.5 for L_2 and 1.1 for L_∞). As shown in Fig. 5g, the temporal convergence order was found to be between first and second order ($L_2 = L_\infty = 1.3$) for inverse map and velocity field. Additionally, in Appendix C we report the convergence of incompressibility errors in the solid, again found to be consistent with the above rates.

Overall the results of this section validate our algorithm against an extensive range of benchmarks, showing the accuracy and robustness of our numerical scheme and its implementation. These results are complemented by a detailed convergence analysis which is found to be consistent with the employed discrete operators and across physical scenarios. Critically, we demonstrated how our formulation naturally allows for the seamless inclusion of a variety of physical phenomena within a consistent framework, preserving stability, accuracy and convergence properties, thus enhancing usability and utility. In the next section we expand on this, further illustrating the wide scope of our solver in a range of multi-physics, complex problems.

6. Numerical results: multi-physics illustrations

Next, we highlight the versatility of our solver by demonstrating a range of potential applications. These include elasticity-induced viscous streaming phenomena, dynamic collision response of a cylinder falling under gravity on a soft trampoline, dynamic and heat transfer characterization of an elastic flag flapping in the wake of a hot cylinder and interaction between multiple, activated, self-propelling soft swimmers. Before proceeding with the illustrations, we recall the key dimensionless parameters Eq. 54 that govern the dynamics of these systems, along with their physical interpretations—Re (Reynolds number) defined as the ratio of inertial to viscous forces, Cau (Cauchy number) as the ratio of inertial to elastic forces, and Er (Ericksen number) as the ratio of viscous to elastic forces.

6.1. Elasticity-induced viscous streaming

Here we demonstrate the ability of our solver to successfully capture second order flow physics effects and rectification phenomena, through the example of viscous streaming. Viscous streaming refers to the time-averaged steady flow that
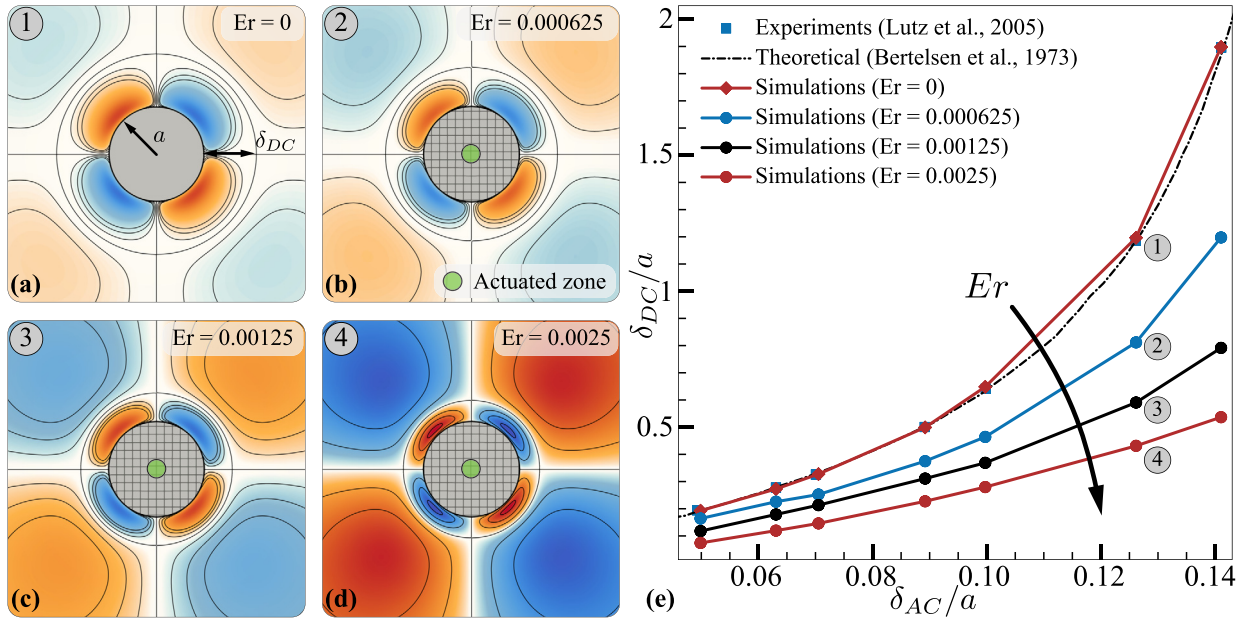
Fig. 6. Elasticity-induced viscous streaming. Case setup for (*a*) rigid cylinder and (*b*) visco-hyperelastic cylinder. Both the cylinders are density matched with the fluid ($\rho_e = \rho_r = \rho_f = 1$), have radius $a = 0.125$, and are placed at (0.5, 0.5) in the computational domain. The parametric values for the imposed motion $x(t) = x(0) + \epsilon a \sin(\omega t)$ with characteristic velocity $V_0 = \epsilon a \omega$ are $x(0) = 0.5$, $\epsilon = 0.1$ and $\omega = 32\pi$. The rigid cylinder is modeled as a Brinkman solid while the visco-hyperelastic cylinder is modeled as a neo-Hookean solid with shear modulus G ($c_1 = 2G$) and internal dissipation $\mu_s = \mu_f$. The actuation zone for the elastic solid is a cylinder with radius $r = 0.2a$ and we did not see appreciable changes when varying this radius r. Parametric values of μ_f and G are determined based on the following key non-dimensional parameters: $\delta_{AC}/a = (\mu_f/\rho_f \omega)^{1/2}/a$ and $Er = \mu_f V_0/Ga$. The computational parameters are set to LCFL = CFL = 0.1 with a spatial resolution of 1024×1024. Time averaged streamline patterns (blue/orange represent clockwise/anti-clockwise rotating regions) depicting streaming response at $R_s = 0.63$ ($\delta_{AC}/a = 0.126$) with increasing values of Er: (*a*) rigid body ($Er = 0$), (*b*) $Er = 0.000625$, (*c*) $Er = 0.00125$ and (*d*) $Er = 0.0025$. The upper bound of Er is chosen such that a finite thickness DC layer is observed. (*e*) Comparison of normalized DC boundary layer thickness δ_{DC}/a vs. normalized AC boundary layer thickness δ_{AC}/a of our simulations (red diamonds) against experiments (blue squares [15]) and theory (black dotted [110]), along with variation of the boundary layer scaling for different Er values (blue, black and red circles). The shear modulus G falls in the range [30, 1000] with variations in δ_{DC}/a and Er.

arises when an immersed body of characteristic length scale a undergoes small-amplitude oscillations (compared to a) in a viscous fluid. This phenomenon has found application in modern inertial microfluidics, as an efficient, controllable mechanism for particle manipulation and sorting [15–17]. Viscous streaming has been well explored and characterized theoretically, experimentally and computationally for rigid shapes of constant curvature such as cylinders or spheres [15, 109–114], and more recently in settings involving complex rigid geometries of multiple curvatures [112,115,116]. Yet, little is known regarding the streaming response to elastic body oscillations, a potentially important aspect in scenarios involving biological materials [28,117]. Motivated by this, we first attempt to numerically recover the classic 2D rigid cylinder solution, to then explore the effect of elasticity in the steady flow response.

Fig. 6a,b highlight the physical setup—a circular rigid or visco-hyperelastic cylinder of radius a is placed at the center of a square domain with unbounded boundary conditions, under quiescent flow conditions. We then impose a small amplitude oscillatory motion $x(t) = x(0) + \epsilon a \sin(\omega t)$ with characteristic velocity $V_0 = \epsilon a \omega$, where ϵ and ω are the non-dimensional amplitude and angular frequency, respectively. In the rigid body limit, the cylinder is formulated as a Brinkman solid and the entire body is actuated with the above motion. For the visco-hyperelastic cylinder instead, the same motion is imposed on a small actuation zone at the center of the cylinder (Fig. 6b, green). We achieve this through Brinkman penalization, which models this zone as a rigid inclusion, allowing us to kinematically *pin* the motion. The system starts from rest in a stress free state and the simulation is run well beyond the initial transient phase until steady state rectified streaming patterns emerge. Further details can be found in the figure caption.

We first characterize the viscous streaming response observed for a rigid cylinder. Following Stuart [109], we characterize streaming response through the streaming Reynolds number $R_s := V_0^2/\nu\omega$, based on the oscillatory Stokes boundary layer thickness, also known as the AC boundary layer thickness $\delta_{AC} := (\nu/\omega)^{1/2}$, where ν is the kinematic viscosity of the fluid. Fig. 6a shows the time averaged streamline patterns for this case, depicting the streaming response for $R_s = 0.63$ ($\delta_{AC}/a = 0.126$), as clockwise (blue) and anti-clockwise (orange) vortical flow structures around the cylinder. We note the presence of a well defined boundary layer of thickness δ_{DC}, also known as the DC boundary layer, commonly used to characterize the topology of streaming flows. The normalized DC layer thickness δ_{DC}/a and the AC layer thickness δ_{AC}/a, can be analytically related as illustrated in Fig. 6e. As seen from this figure, our numerical results [112] compare well with previous boundary layer scalings based on theory [110] and experiments [15].

Following this rigid body–fluid coupling validation for viscous streaming, we perform a cursory exploration to observe the effect of cylinder elasticity on the streaming response, by varying the Ericksen number $Er := \mu_f V_0 / Ga$, where μ_f is the dynamic viscosity of the fluid and G is the shear modulus of the cylinder. Fig. 6b–d present the streaming response for increasing values of Er, at $R_s = 0.63$ ($\delta_{AC}/a = 0.126$). When compared to the rigid body ($Er = 0$) case, the flow structures appear topologically similar, though a decrease in DC layer thickness δ_{DC}/a is observed for increasing values of Er, or equivalently with increasing *softness* of the cylinder. Similar trends are observed for different values of R_s (or δ_{AC}/a) as seen in Fig. 6e, with the boundary layer scaling curves becoming less steep (i.e. higher deviation from the rigid body limit) with increasing Er. Therefore, perhaps counterintuitively, the strength of the DC layer increases as the body stiffness decreases, providing a novel avenue for flow manipulation as well as a potential technique to estimate solid material properties via flow analysis. A rigorous explanation/rationale for this behavior is beyond the scope of the current work and is left as a topic for future research.

6.2. Rigid cylinder bouncing on an elastic trampoline

We now showcase our solver's ability to capture interactions between density mismatched rigid and elastic solids of density ρ_s immersed in a fluid medium with density ρ_f. We begin, as shown in Fig. 7a, by initializing a dense rigid cylinder ($\rho_s = 1.1\rho_f$) of diameter D under a gravity field $-g\,\hat{\boldsymbol{j}}$ in an unbounded domain, at some distance from a horizontal, dense ($\rho_s = 1.1\rho_f$), elastic trampoline of length L, clamped at the end points. We clamp the trampoline dynamically using an external body force applied to the circular tether regions (green zones in Fig. 7a) of the form

$$\boldsymbol{b}(\boldsymbol{x}, t) := \boldsymbol{f}_{\text{tether}}(\boldsymbol{x}, t) = k_{\text{tether}} H_{t\epsilon} \left(r_{\text{tether}} - r(\boldsymbol{x}) \right) \left(\boldsymbol{x} - \boldsymbol{\xi}(\boldsymbol{x}, t) \right)$$

which mimics a compact, conservative spring force. Here k_{tether} denotes the spring stiffness, $H_{t\epsilon}$ is the tether's mollified Heaviside function with mollification width ϵ, r_{tether} is the tethering radius and $r(\boldsymbol{x})$ is the radial distance from the tether point. Additional geometric and parametric details can be found in the figure caption. This dynamic mode of tethering, in addition to the kinematic mode seen earlier in Section 6.1, further illustrates the flexibility of our solver to account for a variety of boundary conditions. We then let the cylinder fall and observe the fluid–solid system's response in time (Fig. 7d–f), while varying (in separate simulations) the trampoline elasticity G, through $Cau := \rho_s Dg/G$ (Fig. 7g–i), and dynamic viscosity $\mu = \mu_f = \mu_s$, through $Er := \mu\sqrt{Dg}/GL$ (Fig. 7j–l).

First, we focus on the system dynamics, visualized through vorticity and inverse map contours in Fig. 7d–f (see video provided in Appendix F). Here we select a representative set of parameters characterized by $Er << 1$ and $Cau \sim O(1)$. In this scenario, as the cylinder approaches the trampoline, stresses propagate through the fluid causing the trampoline to deform even before contact takes place. Concurrently, a vortex sheet at the trampoline surface forms in response to the cylinder's dipolar vortices and the shear stresses induced by the evacuating interstitial fluid film (Fig. 7d) [118]. Eventually, the fluid film is entirely squeezed out and the cylinder collides with and sticks to the trampoline. This in turn causes the cylinder–trampoline system to start oscillating in the vertical direction (Fig. 7e). Meanwhile, the trampoline's vortex-sheets and the cylinder's dipolar vorticity merge, laterally ejecting two symmetric vortex pairs (Fig. 7f), which are eventually deflected upwards by the oscillating trampoline.

We then investigate how this base case scenario varies as a result of changes in Cau, from a *hard* $Cau = 0.32$ (more rigid) to a *soft* $Cau = 1.29$ trampoline. We track the y-coordinate of the COM of the cylinder and trampoline and report it in Fig. 7b. The corresponding vorticity and inverse map snapshots at the final time are reported in Fig. 7g–i. As expected, the harder trampoline (high G, low Cau) does not deform much (blue line, Fig. 7b), but oscillates at a higher frequency (which we expect from the scaling $\omega_{\text{osc}} \sim \sqrt{G/\rho_s}/L$). Instead, as we increase softness, the trampoline oscillates with smaller frequency but deforms more (red line, Fig. 7b), which leads to the ejection of the prominent vortex pairs seen in Fig. 7i.

Next, we plot the vorticity and inverse map contours of final time $t/T \approx 27$, as we vary fluid viscosity from $Er \cdot 10^4 = 0.76$ to $Er \cdot 10^4 = 3.06$ (Fig. 7j–l). We observe stark differences in the vorticity contours—as expected, the vortex pairs are stronger for a less viscous fluid and become more diffused as viscosity increases. However these differences do not affect the system's COM characteristics, which almost perfectly overlap, as seen from Fig. 7c. We conclude that within the range of parameters investigated, Cau (elasticity) dominates Er (viscosity) in determining the system dynamics.

6.3. Elastic flag flapping in the wake of a rigid heated cylinder

Here we demonstrate the multiphysics capabilities of our solver, through the case of an elastic flag flapping in the wake of a rigid heated cylinder. Along with dynamical characterization of the flow-structure interaction, we also characterize the system from a heat transfer perspective. Additionally, through this case we also highlight one of the important aspects of remeshed vortex method—relaxed timestep restriction compared to conventional CFL bounds.

We begin, as shown in Fig. 8a, by initializing a fixed rigid cylinder of diameter D immersed in constant, unbounded, background free stream of velocity $V_\infty \hat{\boldsymbol{i}}$. A density matched ($\rho_e = \rho$) elastic flag of length L is initialized at some distance downstream from the cylinder. We clamp the flag dynamically using a tethering force (Section 6.2, green zone in Fig. 8a) at the upstream end, allowing the flag to flap freely in response to the surrounding flow. Additional geometric and parametric details can be found in the figure caption. Following the description of the solid–fluid coupling setup, we then present the
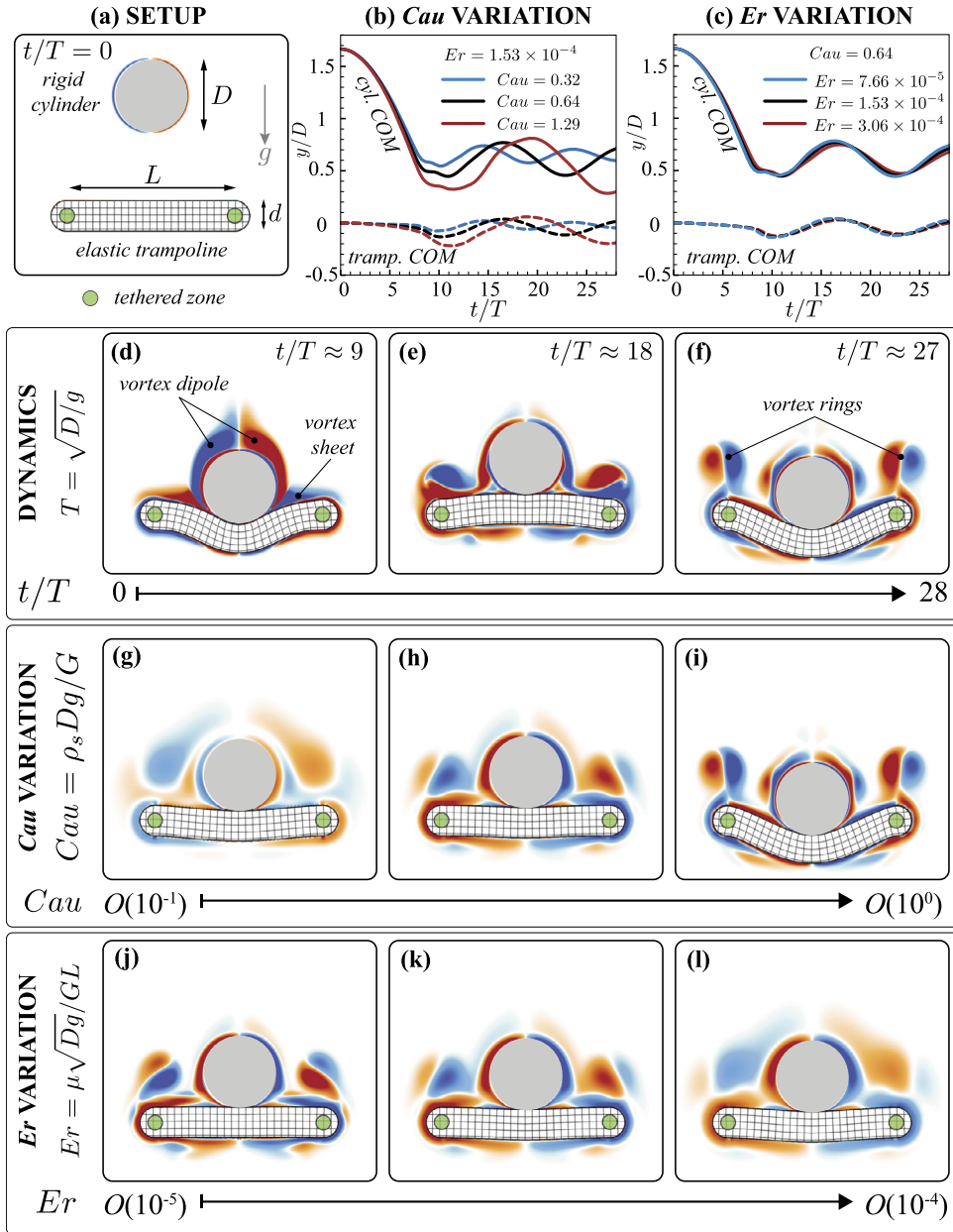
Fig. 7. Rigid cylinder–elastic trampoline collision interaction: (*a*) setup showing the initial snapshot. The rigid cylinder with $\rho_s = 1.1\rho_f$ and diameter $D = 0.24$ is initialized at $(0.5, 0.7)$. The details of the trampoline's exact geometry is deferred to the appendix, here we only list the important parameters. It has the same density as the cylinder, and is initialized with centerline at $y = 0.3$, with length between the anchors $L = 0.56$ and a thickness $d = 0.1$, i.e. $L/d = 5.6$. The tethering zones are centered at both ends of the trampoline length L and has a radius $r_{tether} = 0.025$ i.e. $r_{tether}/t = 0.25$. Both these solids are immersed in a fluid with fixed density ρ_f and a case dependent dynamic viscosity $\mu = \mu_f$, under a gravity field $-g\,\hat{\boldsymbol{j}} = -49.05\,\hat{\boldsymbol{j}}$. The trampoline is made from a visco-elastic neo-Hookean material with case dependent $G = 2c_1$ and same dynamic viscosity as the fluid $\mu_s = \mu_f$. The spring stiffness k_{tether} is set to $10^{-2}\rho_s(\Delta t)^{-2}$ which ensures that the tether's natural frequency is $10\times$ less than the one imposed by the simulation time-step Δt. The tethering H is mollified by $\epsilon = 2h$, where h is the grid spacing. Furthermore, we enable collision forces between the solid bodies with $\epsilon_{coll} = 8h$ and $k_{coll} = 1 \cdot G$. The key non-dimensional parameters in this case are $t/T := t/\sqrt{D/g}$, $Cau := \rho_s Dg/G$ and $Er := \mu\sqrt{Dg}/GL$. All simulations are run till $t/T = 28$. Other computational parameters are $h = (1024)^{-1}$, LCFL $= 0.05$, CFL $= 0.1$. (*b*) Variation of cylinder and trampoline y COM with elasticity $Cau = 0.32$ (blue), 0.64 (black), 1.29 (red) shows significant differences compared to (*c*) variation with dynamic viscosity $Er \cdot 10^4 = 0.76$ (blue), 1.53 (black), 3.06 (red), thus revealing the importance of Cau in determining the system dynamics within the parameter space investigated here. (*d-f*) Depicts the temporal evolution of vorticity (colored, orange and blue indicate positive and negative vorticity respectively) and inverse map (black line) contours for a reference case with $Cau = 1.29$, $Er \cdot 10^4 = 1.53$, showing the deformation of the trampoline and eventual ejection of symmetric vortex pairs due to collision. (*g-i*) Shows vorticity and inverse map snapshots at $t/T \approx 27$ for varying $Cau = 0.32, 0.64, 1.29$ at fixed $Er \cdot 10^4 = 1.53$—differences can be seen in the trampoline's flexural behavior and vorticity evolution. (*g-i*) Illustrates snapshots at $t/T \approx 27$ for varying $Er \cdot 10^4 = 0.76, 1.53, 3.06$ at fixed $Cau = 0.64$, where appreciable differences can be observed only in the vorticity profiles.
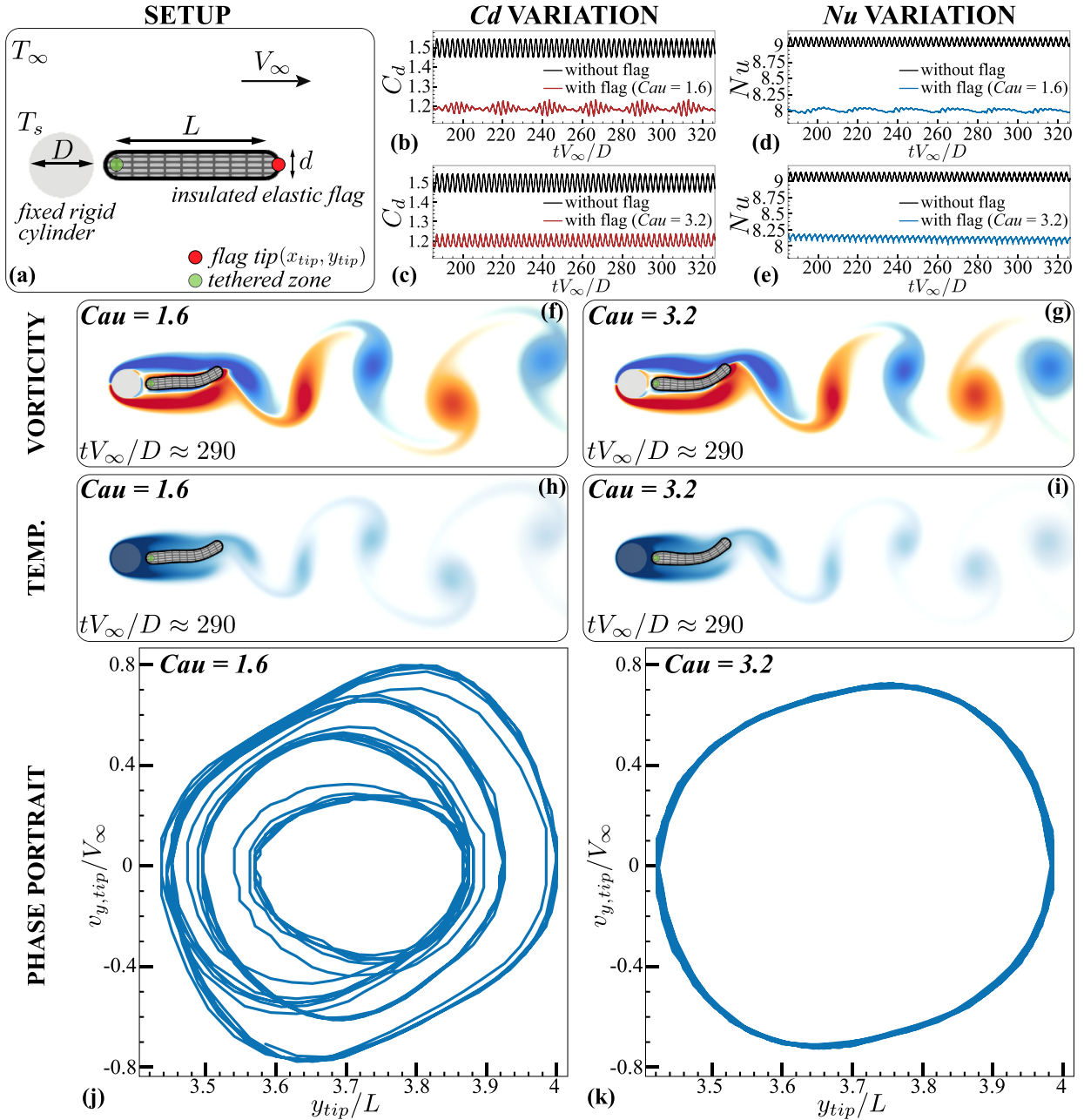
Fig. 8. Elastic flag flapping in the wake of a rigid heated cylinder. (*a*) Setup. The rigid cylinder with diameter $D = 0.06$ is initialized at $(0.1, 0.5)$, and heated to a constant temperature $T_s = 10$. The details of the flag's exact geometry is deferred to the appendix, here we only list the important parameters. It is density matched, and is initialized at $y = 0.5$, with length between the anchors $L = 0.135$, thickness $d = 0.024$ ($L/d = 5.625$), and is thermally insulated with initial temperature equaling the ambient temperature $T_\infty = 0$. The tethering zone is centered at the left end of the flag length L and has a radius $r_{tether} = 0.006$ i.e. $r_{tether}/d = 0.25$. Both these solids are immersed in a fluid with fixed density ρ_f, a case dependent dynamic viscosity $\mu = \mu_f$ and thermal diffusivity α. The fluid has a background free stream horizontal velocity $V_\infty = 4$ and ambient temperature T_∞. The flag is made from a visco-elastic neo-Hookean material with case dependent $G = 2c_1$ and same dynamic viscosity as the fluid $\mu_s = \mu_f$. The spring stiffness k_{tether} is set to $10^{-2}\rho_s (\Delta t)^{-2}$ which ensures that the tether's natural frequency is 10 times less than the one imposed by the simulation time-step Δt. The tethering H is mollified by $\epsilon = 2h$, where h is the grid spacing. The key non-dimensional parameters are tV_∞/D, $Cau := \rho_s V_\infty^2/G$, $Re := \rho_f V_\infty D/\mu_f$ and Prandtl number $Pr := \mu_f/\rho_f \alpha$. For all cases, we fix $Re = 200$ and $Pr = 1$. All simulations are run till $tV_\infty/D = 330$. Other computational parameters are $h = (1024)^{-1}$, $LCFL = CFL = 0.1$. (*b*) Comparison of the temporal drag coefficient C_d profiles against the baseline no flag case for system with $Cau = 1.6$ flag and (*c*) $Cau = 3.2$ flag. (*d*) Comparison of the temporal Nusselt number Nu profiles against the baseline no flag case for $Cau = 1.6$ flag and (*e*) $Cau = 3.2$ cases. (f-i) Snapshots of vorticity field (orange and blue indicate positive and negative vorticity respectively), temperature field (darker shade of blue corresponds to a higher temperature) and inverse map (black line), for $tV_\infty/D \approx 290$, depicting the flag flapping motion and vortex shedding for $Cau = 1.6$ and $Cau = 3.2$ cases. Vorticity, carrying *pockets* of high temperature, is shed in a periodic or quasi-periodic fashion from the cylinder–flag system depending on flag elasticity. (*j*) Phase portrait (i.e. tip velocity vs. deflection) of the flag tip motion plotted over time $tV_\infty/D := 180 - 330$, shown for $Cau = 1.6$ and (*k*) $Cau = 3.2$.

setup of the coupled heat transfer problem and associated governing equations. The cylinder is maintained at a constant temperature T_s while submerged in a viscous fluid of initial ambient temperature T_∞ and constant thermal diffusivity α. The elastic flag is initially at the ambient temperature T_∞ but is thermally insulated and hence does not permit any heat transfer (zero heat flux) across its boundary. We denote by Ω_r and $\partial\Omega_r$ the support and boundary of the cylinder, while Ω_e and $\partial\Omega_e$ stand for the support and boundary of the flag. The outward normal vector of the flag boundary is denoted by $\boldsymbol{n}$. The temperature field $T(\boldsymbol{x}, t)$ is then described by the scalar advection–diffusion equation with corresponding boundary conditions

$$
\begin{aligned}
\frac{\partial T}{\partial t} + (\boldsymbol{v} \cdot \nabla)\, T &= \alpha \nabla^2 T, & \boldsymbol{x} &\in \Sigma \setminus \Omega_r \setminus \Omega_e \\
T &= T_s, & \boldsymbol{x} &\in \partial\Omega_r \\
\nabla T \cdot \boldsymbol{n} &= 0, & \boldsymbol{x} &\in \partial\Omega_e \\
T(\boldsymbol{x}, t=0) &= T_\infty, & \boldsymbol{x} &\in \Sigma \setminus \Omega_r
\end{aligned}
\tag{60}
$$

We solve the governing equations above by extending the penalization technique for a passive scalar field, similar to the methods described in [119,120], by solving the following modified equations between steps 42 and 43 of the main algorithm

$$
\begin{aligned}
\frac{\partial T_\lambda}{\partial t} + \left[H(\phi_r)\boldsymbol{V}_r + (1 - H(\phi_r))\,\boldsymbol{v} \right] \cdot \nabla T_\lambda &= \lambda H(\phi_r)(T_s - T) + \nabla \cdot \left([\alpha(1 - H(\phi_e)) + \eta_\lambda H(\phi_e)] \nabla T_\lambda \right), & \boldsymbol{x} &\in \Sigma \\
T_\lambda(\boldsymbol{x}, t=0) &= T_\infty, \quad \boldsymbol{x} \in \Sigma \setminus \Omega_r \\
T_\lambda(\boldsymbol{x}, t=0) &= T_s, \quad \boldsymbol{x} \in \Omega_r
\end{aligned}
\tag{61}
$$

where T_λ, $\boldsymbol{V}_r$, λ, η_λ, ϕ_r and ϕ_e correspond to the penalized temperature field, rigid body velocity of the cylinder, Brinkman penalization factor, penalized diffusion parameter (Kadoch et al. [120], set equal to 10^{-7}), level set capturing the cylinder boundary $\partial\Omega_r$ and level set capturing the flag boundary $\partial\Omega_e$, respectively. We note that since the cylinder is fixed, $\boldsymbol{V}_r = 0$. The Dirichlet condition on the cylinder (fixed temperature T_s) is imposed via the first term on RHS of Eq. 61, while the Neumann condition (zero heat flux) for the flag boundary is achieved by imposing a vanishing diffusivity inside the flag via the penalized diffusion term [119,120] (second term on RHS). This formulation adds to the flexibility of our solver by accounting for a variety of boundary conditions from a multiphysics perspective. Numerically all operators are discretized similar to the Cauchy momentum equation, described in Section 4.

We simulate this cylinder–flag system long enough after shedding vortices to eventually reach a dynamic, quasi-steady state. This is visualized through vorticity and temperature contours at a particular time instance, for two flags of different elasticities G, in Fig. 8f–i. In this state, we characterize the dynamical and thermal response of the system as functions of flag elasticity G ($Cau = \rho V_\infty^2 / G$), by tracking the resulting drag coefficient C_d and the Nusselt number Nu

$$
C_d := \frac{2|F_{D,x}|}{D V_\infty^2}; \quad Nu := \frac{|Q| D}{(T_s - T_\infty) A \alpha}
\tag{62}
$$

where A is the cylinder heat transfer area, $F_{D,x}$ is the horizontal component of the drag force $\boldsymbol{F}_D$ acting on the cylinder, and Q is the heat transfer rate from the cylinder. We compute these quantities by integrating the penalization term [58,74,121] as shown below

$$
\boldsymbol{F}_D = \lambda \int_\Sigma H(\phi_r)(\boldsymbol{v}_\lambda - \boldsymbol{V}_r)\, d\boldsymbol{x}; \quad Q = \lambda \int_\Sigma H(\phi_r)(T_\lambda - T_s)\, d\boldsymbol{x}
\tag{63}
$$

We first compare the response seen in these cases to a baseline case in which the flag is absent. Fig. 8b,c and Fig. 8d,e present the comparison of temporal C_d and Nu profiles for systems with elastic flag corresponding to $Cau = 1.6$ and $Cau = 3.2$ (i.e. stiff vs. soft), against the baseline case (which has been validated in Appendix E against [122,123]). In both cases, we observe a drop of $\sim 20\%$ in C_d and $\sim 10\%$ in Nu values upon placing an elastic flag in the wake of a cylinder, meaning that the presence of a flag is favorable in terms of cylinder drag, while detrimental to its heat transfer properties. The flag's elasticity Cau negligibly alters the values of these diagnostic quantities but significantly affects their temporal response—while the baseline seems to exhibit a cyclic sinusoidal behavior, the *soft* ($Cau = 3.2$) flag induces a cycle asymmetry which gets amplified for a *hard* ($Cau = 1.6$) flag. To further investigate the dynamical behavior of the system in these cases, we temporally track the vertical flapping motion of the flag at its tip location (red circle in Fig. 8a) and plot the phase portrait of tip velocity vs vertical displacement in Fig. 8j,k. From these plots, we infer that the *soft* ($Cau = 3.2$) flag dynamics, reflected as a limit cycle in the phase portrait, is periodic. The *hard* ($Cau = 1.6$) flag's dynamics is reflected in the phase portrait as a quasi-cycle (an approximate cycle, that does not repeat exactly), indicating its quasi-periodic nature. Similar dynamical transitions with variation in elasticity of flapping flags have been previously reported [48,124]. Such variation in dynamics, drag and thermal response, regulated by introducing and varying elasticity, hint towards potential future applications in drag reduction, heat transfer and associated areas.

We conclude this investigation by observing algorithmic speedups achieved by employing a relaxed LCFL time step restriction. We report $\sim 2\times$ larger timesteps, compared to a simulation whose time step Δt is restricted by the free stream CFL criterion. This is consistent with the speedup expected from the physics of such advection dominated problems. Indeed, for $Re \gg 1$ and $Cau > 1$, the Δt restriction due to the free stream CFL condition ($\Delta t_{\mathrm{CFL}} = \mathrm{CFL}\, h/V_\infty$) is more stringent than its counterpart based on the solid shear wave speed ($\Delta t_{sh} = \mathrm{CFL}\, h\sqrt{\rho/G}$) such that Δt_{sh} is $\sim \sqrt{Cau} \times$ larger than Δt_{CFL}. Our implementation based on remeshed vortex method can sidestep this Δt_{CFL} restriction. Moreover, in the advection dominated cases of this section, the Δt based on LCFL is empirically found to be consistently larger than Δt_{sh}, allowing for timestep speedups of at least $\sim \sqrt{Cau} \times$, which amounts here to $\sim 2\times$. These considerations further compound the virtues of our approach, on top of its accuracy, versatility and relative simplicity.

6.4. Active soft self-propelling swimmers

Finally, in our last demonstration we showcase the ability of our method to seamlessly incorporate endogenous muscular actuation, a feature of importance in bio-locomotion and biophysical settings, through the example of self-propelling swimmers. We consider single and multiple density matched ($\rho_f = \rho_s = \rho$) elastic swimmers of dimension L, resembling the two-dimensional cross-section of a jellyfish, submerged in fluid with dynamic viscosity μ as shown in Fig. 9(a). Within each of these swimmers, we have an activated region that mimics the action of localized, internal muscles. We utilize the formulation of Section 3.5 and actuate this region by using the following time-periodic activation map $\boldsymbol{\eta}_s$

$$\boldsymbol{\eta}_s\left(\boldsymbol{X} := \begin{pmatrix} X \\ Y \end{pmatrix}, t\right) := \begin{pmatrix} X e^{\lambda_s Y H_\varepsilon(\phi_a)\sin^8(\omega t)} \\ (1 - e^{-\lambda_s Y H_\varepsilon(\phi_a)\sin^8(\omega t)})/\lambda_s \end{pmatrix} \tag{64}$$

where $H_\varepsilon(\phi_a)$ is the indicator function of the active region, meant to localize the effects of $\boldsymbol{\eta}_s$ and ω is the angular frequency. The symbol λ_s here indicates a stretch factor—indeed $\boldsymbol{\eta}_s$ stretches and compresses elements away from the swimmer centerline, while maintaining incompressibility (i.e. $\det(\nabla \boldsymbol{\eta}_s) \equiv 1$, see Fig. 9(b) and corresponding caption). The surrounding unactivated solid region is passive and responds to the effects of the activation above. The elastic modulus of both the activated and unactivated regions is denoted by G. We note that similar setups were investigated before qualitatively [42,85], but not quantitatively. Here, we complement previous studies with a rigorous quantitative characterization, for reproducibility.

We begin by observing the locomotion of a single swimmer of length L, for a representative case with $Cau := \rho\omega^2 L^2/G = 0.064$ and $Er := \mu\omega/G = 8.04 \cdot 10^{-4}$. The swimmer flaps its appendages and moves upward, causing the generation and shedding of trailing vortices as shown in Fig. 9(e). The region of activation is highlighted in gray. We track the swimmer COM coordinates and velocities and report them in Fig. 9(c) and Fig. 9(d), respectively. These plots indicate that the swimmer follows a perfectly vertical trajectory due to symmetry. We observe the $Re := V_{\max}L/\nu$ to be ≈ 20, based on the maximum velocity $V_{\max}$ during the course of the swimmer's trajectory. We note that even though the actuation is periodically symmetric, the resulting forward speed is periodically asymmetric with noticeable accelerations during the power stroke. This break in temporal symmetry, which helps propel the swimmer faster, arises due to elastic relaxation time scales pervasive throughout the swimmer body. The motion then emerges due to a complex interplay between actuation, elasticity and morphology, whose parametric details can be found in the figure caption.

Next, we place three swimmers in a triangular formulation, with one adult *leader* jellyfish and two juvenile *followers*. The leader has the same proportions as the single swimmer in the simulations above. Both followers are scaled down versions of the leader (parametric details can be found in the figure caption). We activate each of these swimmers similar to the previous case. In this case, the flow-mediated collective behavior leads to complex dynamics as seen from Fig. 9(f). We first focus on the followers. Their trajectory is significantly affected by the vorticity shed by the leader. They are first drawn closer together towards the symmetry axis, shortly after which they closely approach and *kiss* the leader's appendages. Due to this near-approach event, they make a near-perpendicular 90° turn and continue propelling in the horizontal direction. Meanwhile the leader persists on its expected straight, vertical trajectory, seemingly unaffected by the followers. On a closer comparison with the trajectory of an equivalent single swimmer (i.e. without the followers), we see that it is slowed down (Fig. 9(c)). The rationale for this behavior is uncovered from the vertical velocity v_y plots of Fig. 9(d). For $t/T < 3$ the followers, which are in close proximity to the leader, slow it down (solid black line vs. dashed black for a single swimmer). Once the leader frees itself from the followers' influence, it swims with the same speed as the single swimmer, seen for $t/T > 4$.

Finally, we draw attention to the preservation of symmetry in the swimmer trajectories (in Fig. 9(d)) and the flow fields of Fig. 9(f), even after long times and a critical near-approach event. This, along with a battery of tests and illustrations, attests to the accuracy and robustness of our FSI approach.

7. Conclusion

In conclusion, we have presented a unified framework based on remeshed vortex method for the simulation of mixed rigid/elastic bodies immersed in a viscous fluid. Our approach seamlessly incorporates a rigid body-fluid interaction formulation based on Brinkman penalization and projection, within a broader elastic body-fluid methodology based on inverse map
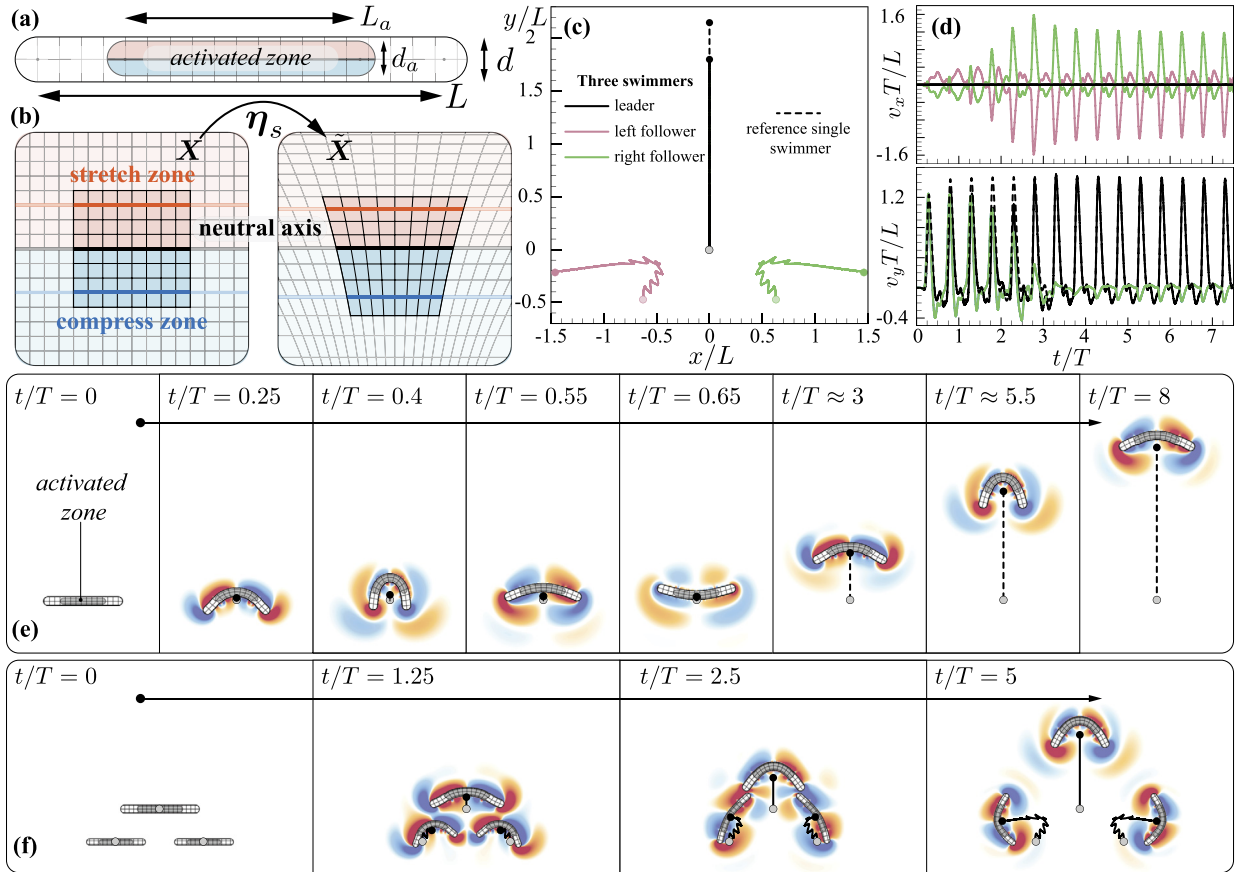
Fig. 9. Single and multiple swimmers (*a*) Setup: an active, elastic swimmer of density $\rho = 1$, elastic modulus $G = 2.5$ resembling a jellyfish is immersed in a fluid of density $\rho = 1$, dynamic viscosity $\mu = 1e^{-3}$. The details of exact geometry of the swimmer is deferred to the appendix, here we only list the important parameters. We initialize it with length $L = 0.2$ and thickness $d = 0.024$, i.e. $d/L = 0.12$. The swimmer has an active region with exactly the same geometry but different parameters $L_a = 0.112 = 0.56L$ and $d_a = 0.0168 = 0.7d$, i.e. $d_a/L_a = 0.15$. This active region accommodates a time-periodic incompressible activation map $\boldsymbol{\eta}_s$ of Eq. 64 with λ_s set to $\log(2.2)/(d_a/2)$ which indicates a maximum elemental stretch/compression of $2.2\times$ (see below) and $\omega = 2\pi/3.125$. This results in the following non-dimensional parameter set $Cau := \rho\omega^2 L^2/G = 0.064$ and $Er := \mu\omega/G = 8.04 \cdot 10^{-4}$. (*b*) Schematic presenting the effects of this map $\boldsymbol{\eta}_s$ on a regular Cartesian grid. We first demarcate the centerline neutral axis (solid black) upon which the map has no effect. Above the neutral axis resides the *stretching* (red) zone where elements are stretched horizontally while being squished vertically to maintain incompressibility. The amount of stretch λ_s is reflected in the degree of stretch of a material line element marked above in solid red. Simultaneously, below the neutral axis lies the *compression* (blue) zone, where elements are compressed horizontally. Applying this map time-periodically, while preserving polarities of the stretch and compress zones, results in alternate bending and relaxing of the centerline leading to a propulsive motion of the swimmer. The resulting non-dimensional trajectories of single (dashed black line) and multiple (solid lines) swimmers is shown in (*c*), where the initial and final positions are marked with hollow and solid circles respectively. (*d*) Non-dimensional horizontal velocity and non-dimensional vertical velocity of the swimmers as they evolve with time. (*e*) Time-series of snapshots of a single, vertically locomoting swimmer and its gray active region along with vorticity (colored, orange and blue indicate positive and negative vorticity respectively) and inverse map (black line) contours. For reference, the swimmer is initialized at $(0.5, 0.35)$ and is allowed to move till $t/T = 8$. Additionally, the center of mass location with time is highlighted by a dashed black line. (*f*) Showcases a similar time-series, but this time for three similarly activated elastic swimmers—one adult leader and two juvenile followers. The leader has the exact geometry and proportions of the single swimmer of (e) and is initialized at the same location $(0.5, 0.35)$. The juveniles have the same geometry as the leader but are 75% its size. They are initialized symmetrically with the left follower at $(0.375, 0.25625)$ and right follower at $(0.625, 0.25625)$. In this case, we also enabled collision forces between the bodies with $\epsilon_{\text{coll}} = 8h$ and $k_{\text{coll}} = G$. The center of mass histories of the leader, left follower and right follower are marked with a solid black, pink and green lines respectively. The snapshots show the followers closing in towards the symmetry axis, *kissing* the leader and making a hard, right turn to then proceed almost horizontally for the rest of the time. Meanwhile, the leader continues on its vertical upward path. Other pertinent computational parameters are $h = (1024)^{-1}$, LCFL = 0.05, CFL = 0.1.

technique and one continuum formulation. Our formulation produces a neat, relatively simple algorithm, whose accuracy and robustness is demonstrated through rigorous benchmarking and convergence analysis, against a battery of theoretical/numerical tests. Through various multifaceted illustrations (which themselves may serve as detailed benchmarks for future studies), we further demonstrate our solver's versatility, applicability and robustness across multiphysics scenarios, boundary conditions, constitutive and actuation models, along with algorithmic speedup for advection dominated problems. In particular, the broad range of physics captured involving muscular actuation, multi-body contact, self propulsion and heat transfer, illustrates the utility of our method in a variety of applications, from bio-locomotion to microfluidics. The use of particle methods and convenient grid based operators renders the solver scalable and makes it portable to parallel archi-

tecture such as GPUs and multicores [61]. However, opportunities for improvement, both algorithmically and in terms of parallelism, exist. Regarding algorithmic advancements, first we may replace our current mollification approach and resolve the physics near the interface via modified interfacial stencils [125,126], to improve the L_∞ norm convergence now limited to first order. Second, the time step restriction based on shear wave speed inside the elastic solid may be bypassed using an implicit solver [101] or a local time-stepping technique [61]. Regarding advances in parallelism, an implementation able to take advantage of large-scale modern heterogeneous computing infrastructures would be needed to enable the simulation of 3D and/or thousands of immersed elastic/rigid bodies in realistic physical times. All the above directions are avenues of future work.

CRediT authorship contribution statement

Yashraj Bhosale: Conceptualization, Data curation, Investigation, Methodology, Software, Validation, Visualization, Writing – original draft. **Tejaswin Parthasarathy:** Conceptualization, Data curation, Investigation, Methodology, Software, Validation, Visualization, Writing – original draft. **Mattia Gazzola:** Conceptualization, Data curation, Investigation, Methodology, Software, Validation, Visualization, Writing – original draft.

Declaration of competing interest

The authors declare that they have no known competing financial interests or personal relationships that could have appeared to influence the work reported in this paper.

Acknowledgements

Appendix A. Oscillatory response in parallel layers of fluid and solid: density mismatch validation

Here, we showcase our ability to accurately capture effects of density mismatch by once again comparing numerical results to analytical ones in the case of oscillating, parallel sandwiched elastic solid–fluid layers. We retain the physical setup and explanation of Section 5.2, and focus on the results for the density mismatch case $\rho_e = 2$, $\rho_f = 1$. These results are presented in Fig. A.10(a) (black) and contrasted to the density matched results from the main text (red). We clearly see stark differences in the velocity profiles within the solid phase. Once again, maximum differences between analytical and numerical results are seen in the diffuse interface region. Plotting convergence by retaining the corresponding definition of error used in the main text for different temporal instants in Fig. A.10(b) reveals consistent first to second order convergence (1.86 for L_2 and 1.19 for L_∞), as expected.
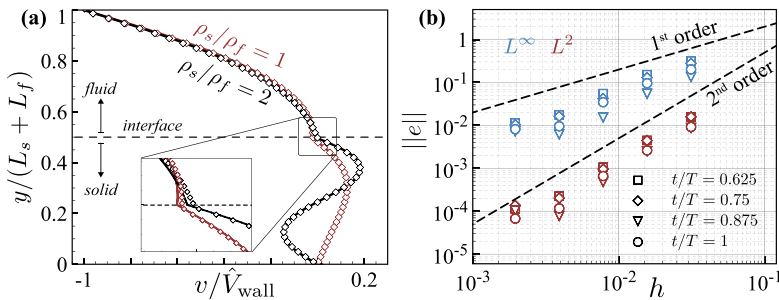

Fig. A.10. Oscillatory response in parallel density mismatched solid–fluid layers for a neo-Hookean visco-elastic solid. We retain the physical setup of Section 5.2 and run simulations to obtain the velocity fields at the center of the domain, shown in (*a*) (black), which once again agrees with the analytical results. We also plot the velocity traces of the corresponding density matched case from the main text in red to contrast it with this case−indeed stark differences are seen within the solid phase. The inset shows the concentration of errors near the diffuse interface. For reference, numerical results are plotted with scatter points whereas analytical results are plotted with a solid line. Tracking these velocity results with changing resolution results in the convergence plot shown in (*b*) where L_∞ (blue) and L_2 (red) norms of the error are plotted against grid spacing h at different t/T. Trends indicate a first to second order convergence as expected. The dynamic parameters corresponding to the fluid phase in this setup are $\rho_f = 1$, $\mu_f = 0.02$. The dynamic parameters of the elastic solid are $\rho_e = 2$, $\mu_e = 0.1\mu_f$ and shear modulus $c_1 = 0.01$ i.e. $G = 2c_1 = 0.02$. The simulations are run until $t/T = 10$, and physical quantities are sampled within the last cycle. The key non-dimensional dynamic parameters for this benchmark are $Re = \rho_f \dot\gamma L_f / \mu_f = 2$, $Er = \mu_f \hat V_{\text{wall}} / 2GL_s = 1$. The computational parameters are set to LCFL $= 0.05$, CFL $= 0.1$.

Appendix B. Details of discretization in inverse-map advection

Here we explain the differences between advecting the reference map $\boldsymbol{\xi}$ using a particle-based and grid-based approach. We begin by noting that the inverse map satisfies the following advection equation on the grid, obtained by discretizing the material derivative [77]

$$\frac{\partial \boldsymbol{\xi}_h}{\partial t} + \boldsymbol{v}_h \cdot \nabla_h \boldsymbol{\xi}_h = 0 \tag{B.1}$$

where the subscript h indicates discrete fields and operators. Meanwhile, particle advection and moment-conserving remeshing solve the conservative form of the advection equation (see Eq. 1,2 in [55], [67])

$$\frac{\partial \boldsymbol{\xi}_h}{\partial t} + \nabla_h \cdot (\boldsymbol{v}_h \otimes \boldsymbol{\xi}_h) = 0. \tag{B.2}$$

For incompressible systems, both these formulations are equivalent. We see this by expanding the second term on the LHS of Eq. B.2, using the identity $\nabla_h \cdot (\boldsymbol{v}_h \otimes \boldsymbol{\xi}_h) := \boldsymbol{v}_h \cdot \nabla_h \boldsymbol{\xi}_h + \boldsymbol{\xi}_h (\nabla_h \cdot \boldsymbol{v}_h)$, as

$$\frac{\partial \boldsymbol{\xi}_h}{\partial t} + \boldsymbol{v}_h \cdot \nabla_h \boldsymbol{\xi}_h + \boldsymbol{\xi}_h (\nabla_h \cdot \boldsymbol{v}_h) = 0 \tag{B.3}$$

which, compared to Eq. B.1, presents the residual term $\boldsymbol{\xi}_h (\nabla_h \cdot \boldsymbol{v}_h)$ on the LHS. This term is exactly zero for incompressible solids and fluids because $\nabla_h \cdot \boldsymbol{v}_h = 0$, and in numerical simulations we could confirm this in the bulk. Nonetheless, at the solid–fluid interface, numerically this term is no longer exactly zero but takes small, localized and bounded non-zero values due to interfacial blending (see the next section Appendix C). Then in this case, the use of particle advection implies the solution of Eq. B.2, not Eq. B.1. This is well recognized within the vortex methods community [55], particularly in solving subsonic compressible flows using vortex particles [67] where additional equations are employed to account for such non-zero dilatation $\nabla_h \cdot \boldsymbol{v}_h$. If we employ vortex methods to solve Eq. B.1 then, we need to similarly introduce additional correction equations accounting for the residual term. Since this correction introduces additional discretization and corresponding computational costs, we use a grid-based approach and directly discretize Eq. B.1 for advecting the inverse-map $\boldsymbol{\xi}$.

Appendix C. Convergence of incompressibility errors inside the solid

For incompressible elastic solids with density ρ_e, incompressibility dictates that the mass of a differential element of the solid should be constant, and therefore locally the determinant of the deformation gradient $det(\boldsymbol{F})$ should be identically equal to 1. As shown in Jain et al. [18], an incompressible velocity field ensures that the above conditions are satisfied, although only in the continuous limit but not necessarily in the discrete limit. We note that a consistent, accurate numerical implementation then produces incompressibility errors that are bounded and convergent. We then demonstrate this robustness and accuracy by presenting the quantification and convergence of incompressibility errors inside the solid, encountered in our method, in the benchmark case of collision between two hyperelastic cylinders immersed in a fluid, illustrated in Section 5.4.

Fig. C.11a-c showcase the qualitative temporal variation of incompressibility errors for one of the solids, captured through contours of $|det(\boldsymbol{F}) - 1|$ field. We observe that this field is bounded and localized in the solid–fluid blur/blending zone around the interface (black contour), at all times. Additionally, incompressibility is ensured within the pure solid zone at all times. In order to quantify and demonstrate convergence for these incompressibility errors we compute two diagnostic quantities following [18,85]. These are the L_2 norm of the $|det(\boldsymbol{F}) - 1|$ field, and the total mass loss of the solid computed as

$$\text{Mass loss} = 1 - \frac{M_e(t)}{M_e(t=0)} = 1 - \frac{\rho_e \int_\Sigma H(\phi_e(t)) \, d\boldsymbol{x}}{\rho_e \int_\Sigma H(\phi_e(t=0)) \, d\boldsymbol{x}} \tag{C.1}$$

where M_e represents the total mass of the solid and ϕ_e is the level set capturing the interface of the body. Fig. C.11d,e present the temporal variation of $||det(\boldsymbol{F}) - 1||_2$ and mass loss, respectively, at different spatial resolutions. We observe that errors increase with deformation, i.e. reach their highest values at maximal deformation ($t \approx 0.3$), and then decrease again or saturate with time to a nearly constant value, hence showing no accumulation of errors over time in the present approach. Additionally, both these diagnostic quantities are seen to converge with spatial resolution. We present this spatial convergence in Fig. C.11f, g, retaining the computational parameters of Section 5.4. As seen from this figure, the convergence order for both diagnostics was found to be between first and second order (least squares fit of 1.2 for $||det(\boldsymbol{F}) - 1||_2$ and 1.5 for mass loss), which is consistent with the spatial discretization of our solver. Thus, our solver is consistent and accurate in ensuring incompressibility in both the solid and fluid phases.
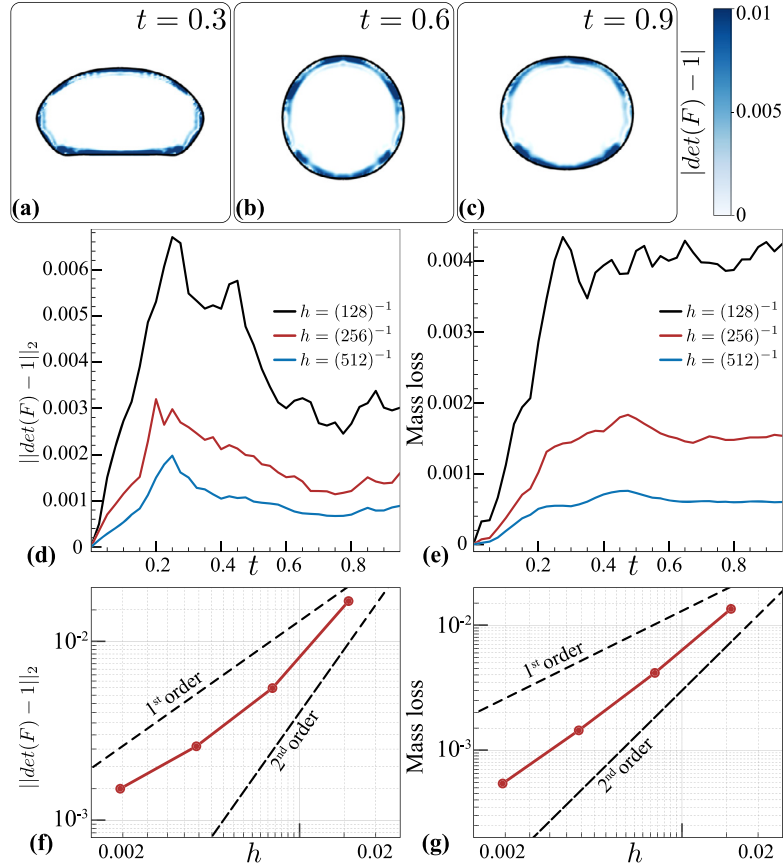
Fig. C.11. Convergence of incompressibility errors inside the solid. (*a-c*) Temporal variation of the $|det(\mathbf{F}) - 1|$ field contours (colored, darker shade of blue represents higher values) for one of the solids from the benchmark illustrated in Section 5.4. Localization of the error can be seen in the solid–fluid blur/blending zone, near the interface (black contour). Computational details can be found in Fig. 5 caption. Temporal variation of (*d*) L_2 norm of $|det(\mathbf{F}) - 1|$ field, $||det(\mathbf{F}) - 1||_2$ and (*e*) mass loss plotted against time t, for different spatial resolutions. Spatial convergence: (*f*) $||det(\mathbf{F}) - 1||_2$ and (*g*) mass loss plotted against grid spacing h, at time $t = 0.3$.

Appendix D. Geometrical details of trampoline, flag and swimmers

The trampoline (Section 6.2), flag (Section 6.3) and swimmers (Section 6.4) shown in the main text are constructed using the same geometry which we now discuss. The geometry is essentially a rounded rectangle—made of a central rectangle with two semi-circles at its ends—with the diameter of the end circles matching the width of the central rectangle. The geometry is characterized by its left center point $\mathbf{x}_c := (x_c, y_c)^T$, the length ($L$) and thickness ($d$) of the rectangle. Its level set function is then described by

$$\phi\left(\mathbf{x} := (x, y)^T\right) := \begin{cases} \sqrt{(x - x_c)^2 + (y - y_c)^2} - d/2 & \text{for } x < x_c \\ |y - y_c| - d/2 & \text{for } x_c \le x \le x_c + L \\ \sqrt{(x - x_c - L)^2 + (y - y_c)^2} - d/2 & \text{for } x > x_c + L \end{cases}$$

Appendix E. Dynamic and thermal validation for flow past a cylinder

Here, we briefly present the validation for the no flag variant (i.e. flow past a rigid cylinder) for the illustration case of elastic flag flapping in the wake of a rigid heated cylinder, described in Section 6.3. In order to validate the dynamical and thermal response, we present a comparison of commonly used diagnostic quantities, which include the mean drag coefficient $\overline{C}_d$, mean Nusselt number $\overline{Nu}$ and the Strouhal number St, against previously published results [122,123]. We compute $\overline{C}_d$ and $\overline{Nu}$ based on Eq. 62, while St is computed as follows

$$St = \frac{fD}{V_\infty} \tag{E.1}$$

where f, D and V_∞ correspond to the vortex shedding frequency, cylinder diameter and free stream velocity, respectively. Table E.1 shows the comparison of the values of the above quantities obtained using our method against those found in previous works for Reynolds number $Re = 200$ and Prandtl number $Pr = 1$. We note that our results show close agreement with the previously published values. For a more detailed validation of this case, the reader is referred to our previous work [58].

Table E.1

Dynamic and thermal validation for flow past a cylinder. Comparison of drag coefficient $\overline{C}_d$, Nusselt number $\overline{Nu}$ and the Strouhal number St computed with the present method against previously published results [122,123] at Reynolds number $Re = 200$ and Prandtl number $Pr = 1$. For computational details, refer to Fig. 8 caption.

	$\overline{C}_d$	$\overline{Nu}$	St
Previous results	1.45	9.05	0.20
Present methods	1.49	9.06	0.19

Appendix F. Animations of simulated cases

We have included animated videos of all cases simulated in the paper, which can be accessed through the following link.

References

[1] S. Alben, M. Shelley, J. Zhang, Drag reduction through self-similar bending of a flexible body, Nature 420 (2002) 479–481.
[2] C. Pozrikidis, Modeling and Simulation of Capsules and Biological Cells, CRC Press, 2003.
[3] S. Alben, M. Shelley, J. Zhang, How flexibility induces streamlining in a two-dimensional flow, Phys. Fluids 16 (2004) 1694–1713.
[4] E.D. Tytell, M.C. Leftwich, C.-Y. Hsu, B.E. Griffith, A.H. Cohen, A.J. Smits, C. Hamlet, L.J. Fauci, Role of body stiffness in undulatory swimming: insights from robotic and computational models, Phys. Rev. Fluids 1 (2016) 073202.
[5] T. Parthasarathy, S.P. Das, Effect of synthetic jet parameters on controlled flow over an airfoil, Fluid Mech. Res. 44 (2017).
[6] A. Goza, T. Colonius, J.E. Sader, Global modes and nonlinear analysis of inverted-flag flapping, J. Fluid Mech. 857 (2018) 312–344.
[7] J. LaGrone, R. Cortez, L. Fauci, Elastohydrodynamics of swimming helices: effects of flexibility and confinement, Phys. Rev. Fluids 4 (2019) 033102.
[8] Y. Bhosale, E. Esmaili, K. Bhar, S. Jung, Bending, twisting and flapping leaf upon raindrop impact, Bioinspir. Biomim. 15 (2020) 036007.
[9] S.-J. Park, M. Gazzola, K.S. Park, S. Park, V. Di Santo, E.L. Blevins, J.U. Lind, P.H. Campbell, S. Dauth, A.K. Capulli, et al., Phototactic guidance of a tissue-engineered soft-robotic ray, Science 353 (2016) 158–162.
[10] X. Zhang, F.K. Chan, T. Parthasarathy, M. Gazzola, Modeling and simulation of complex dynamic musculoskeletal architectures, Nat. Commun. 10 (2019) 1–12.
[11] O. Aydin, X. Zhang, S. Nuethong, G.J. Pagan-Diaz, R. Bashir, M. Gazzola, M.T.A. Saif, Neuromuscular actuation of biohybrid motile bots, Proc. Natl. Acad. Sci. USA 116 (2019) 19841–19847.
[12] M. Gazzola, M. Argentina, L. Mahadevan, Scaling macroscopic aquatic locomotion, Nat. Phys. 10 (2014) 758–761.
[13] M. Gazzola, M. Argentina, L. Mahadevan, Gait and speed selection in slender inertial swimmers, Proc. Natl. Acad. Sci. USA 112 (2015) 3874–3879.
[14] H. Ceylan, J. Giltinan, K. Kozielski, M. Sitti, Mobile microrobots for bioengineering applications, Lab Chip 17 (2017) 1705–1724.
[15] B.R. Lutz, J. Chen, D.T. Schwartz, Microscopic steady streaming eddies created around short cylinders in a channel: flow visualization and Stokes layer scaling, Phys. Fluids 17 (2005) 023601.
[16] P. Marmottant, S. Hilgenfeldt, A bubble-driven microfluidic transport element for bioengineering, Proc. Natl. Acad. Sci. USA 101 (2004) 9523–9527.
[17] R.H. Liu, R. Lenigk, R.L. Druyor-Sanchez, J. Yang, P. Grodzinski, Hybridization enhancement using cavitation microstreaming, Anal. Chem. 75 (2003) 1911–1917.
[18] S.S. Jain, K. Kamrin, A. Mani, A conservative and non-dissipative Eulerian formulation for the simulation of soft solids in fluids, J. Comput. Phys. 399 (2019) 108922.
[19] W.K. Liu, S. Jun, Y.F. Zhang, Reproducing kernel particle methods, Int. J. Numer. Methods Fluids 20 (1995) 1081–1106.
[20] R.A. Gingold, J.J. Monaghan, Smoothed particle hydrodynamics: theory and application to non-spherical stars, Mon. Not. R. Astron. Soc. 181 (1977) 375–389.
[21] D.J. Price, Smoothed particle hydrodynamics: things I wish my mother taught me, arXiv preprint, arXiv:1111.1259, 2011.
[22] M.S. Shadloo, G. Oger, D. Le Touzé, Smoothed particle hydrodynamics method for fluid flows, towards industrial applications: motivations, current state, and challenges, Comput. Fluids 136 (2016) 11–34.
[23] J.A. Sethian, Level Set Methods and Fast Marching Methods, 1999.
[24] W.F. Noh, P. Woodward, Slic (simple line interface calculation), in: Proceedings of the Fifth International Conference on Numerical Methods in Fluid Dynamics, June 28–July 2, 1976, Twente University, Enschede, Springer, 1976, pp. 330–340.
[25] B. Valkov, C.H. Rycroft, K. Kamrin, Eulerian method for multiphase interactions of soft solid bodies in fluids, J. Appl. Mech. 82 (2015).
[26] K. Sugiyama, S. Ii, S. Takeuchi, S. Takagi, Y. Matsumoto, A full Eulerian finite difference approach for solving fluid–structure coupling problems, J. Comput. Phys. 230 (2011) 596–627.
[27] K. Sugiyama, S. Ii, S. Takeuchi, S. Takagi, Y. Matsumoto, Full Eulerian simulations of biconcave neo-hookean particles in a Poiseuille flow, Comput. Mech. 46 (2010) 147–157.
[28] N. Nagano, K. Sugiyama, S. Takeuchi, S. II, S. Takagi, Y. Matsumoto, Full-Eulerian finite-difference simulation of fluid flow in hyperelastic wavy channel, J. Fluid Sci. Technol. 5 (2010) 475–490.
[29] H.H. Hu, N.A. Patankar, M. Zhu, Direct numerical simulations of fluid–solid systems using the arbitrary Lagrangian–Eulerian technique, J. Comput. Phys. 169 (2001) 427–462.
[30] T.E. Tezduyar, M. Behr, S. Mittal, J. Liou, A new strategy for finite element computations involving moving boundaries and interfaces—The deforming-spatial-domain/space-time procedure: II. Computation of free-surface flows, two-liquid flows, and flows with drifting cylinders, Comput. Methods Appl. Mech. Eng. 94 (1992) 353–371.

[31] K. Takizawa, B. Henicke, A. Puntel, T. Spielman, T.E. Tezduyar, Space-time computational techniques for the aerodynamics of flapping wings, J. Appl. Mech. 79 (2012).
[32] H. Watanabe, S. Sugiura, H. Kafuku, T. Hisada, Multiphysics simulation of left ventricular filling dynamics using fluid-structure interaction finite element method, Biophys. J. 87 (2004) 2074–2085.
[33] K. Takizawa, B. Henicke, T.E. Tezduyar, M.-C. Hsu, Y. Bazilevs, Stabilized space–time computation of wind-turbine rotor aerodynamics, Comput. Mech. 48 (2011) 333–344.
[34] H.H. Hu, Direct simulation of flows of solid-liquid mixtures, Int. J. Multiph. Flow 22 (1996) 335–352.
[35] B.E. Griffith, N.A. Patankar, Immersed methods for fluid–structure interaction, Annu. Rev. Fluid Mech. 52 (2020) 421–448.
[36] C.S. Peskin, The immersed boundary method, Acta Numer. 11 (2002) 479–517.
[37] M. Uhlmann, An immersed boundary method with direct forcing for the simulation of particulate flows, J. Comput. Phys. 209 (2005) 448–476.
[38] K. Taira, T. Colonius, The immersed boundary method: a projection approach, J. Comput. Phys. 225 (2007) 2118–2137.
[39] C. Wang, J.D. Eldredge, Strongly coupled dynamics of fluids and rigid-body systems with the immersed boundary projection method, J. Comput. Phys. 295 (2015) 87–113.
[40] A. Goza, T. Colonius, A strongly-coupled immersed-boundary formulation for thin elastic structures, J. Comput. Phys. 336 (2017) 401–411.
[41] L. Zhang, A. Gerstenberger, X. Wang, W.K. Liu, Immersed finite element method, Comput. Methods Appl. Mech. Eng. 193 (2004) 2051–2067.
[42] H. Zhao, J.B. Freund, R.D. Moser, A fixed-mesh method for incompressible flow–structure systems with finite solid deformations, J. Comput. Phys. 227 (2008) 3114–3140.
[43] F.-B. Tian, H. Dai, H. Luo, J.F. Doyle, B. Rousseau, Fluid–structure interaction involving large deformations: 3d simulations and applications to biological systems, J. Comput. Phys. 258 (2014) 451–469.
[44] B.E. Griffith, X. Luo, Hybrid finite difference/finite element immersed boundary method, Int. J. Numer. Methods Biomed. Eng. 33 (2017).
[45] Z. Li, M.-C. Lai, The immersed interface method for the Navier–Stokes equations with singular forces, J. Comput. Phys. 171 (2001) 822–842.
[46] R. Glowinski, T.-W. Pan, T.I. Hesla, D.D. Joseph, J. Periaux, A fictitious domain approach to the direct numerical simulation of incompressible viscous flow past moving rigid bodies: application to particulate flow, J. Comput. Phys. 169 (2001) 363–426.
[47] Z. Yu, A dlm/fd method for fluid/flexible-body interactions, J. Comput. Phys. 207 (2005) 1–27.
[48] T. Engels, D. Kolomenskiy, K. Schneider, J. Sesterhenn, Numerical simulation of fluid–structure interaction with the volume penalization method, J. Comput. Phys. 281 (2015) 96–115.
[49] J.D. Eldredge, Numerical simulation of the fluid dynamics of 2d rigid body motion with the vortex particle method, J. Comput. Phys. 221 (2007) 626–648.
[50] J.D. Eldredge, Dynamically coupled fluid–body interactions in vorticity-based numerical simulations, J. Comput. Phys. 227 (2008) 9170–9194.
[51] J.T. Beale, A. Majda, Vortex methods. I. Convergence in three dimensions, Math. Comput. 39 (1982) 1–27.
[52] A. Leonard, Computing three-dimensional incompressible flows with vortex elements, Annu. Rev. Fluid Mech. 17 (1985) 523–559.
[53] P.-A. Raviart, An analysis of particle methods, in: Numerical Methods in Fluid Dynamics, Springer, 1985, pp. 243–324.
[54] G.-H. Cottet, P.D. Koumoutsakos, et al., Vortex Methods: Theory and Practice, vol. 8, Cambridge University Press, Cambridge, 2000.
[55] G. Winckelmans, Vortex Methods, Encyclopedia of Computational Mechanics, 2004.
[56] P. Koumoutsakos, Multiscale flow simulations using particles, Annu. Rev. Fluid Mech. 37 (2005) 457–487.
[57] M. Coquerelle, G.-H. Cottet, A vortex level set method for the two-way coupling of an incompressible fluid with colliding rigid bodies, J. Comput. Phys. 227 (2008) 9121–9137.
[58] M. Gazzola, P. Chatelain, W.M. Van Rees, P. Koumoutsakos, Simulations of single and multiple swimmers with non-divergence free deforming geometries, J. Comput. Phys. 230 (2011) 7093–7114.
[59] M. Gazzola, W.M. Van Rees, P. Koumoutsakos, C-start: optimal start of larval fish, J. Fluid Mech. 698 (2012) 5–18.
[60] W.M. Van Rees, M. Gazzola, P. Koumoutsakos, Optimal shapes for anguilliform swimmers at intermediate Reynolds numbers, J. Fluid Mech. 722 (2013).
[61] D. Rossinelli, B. Hejazialhosseini, W. van Rees, M. Gazzola, M. Bergdorf, P. Koumoutsakos, Mrag-i2d: multi-resolution adapted grids for remeshed vortex methods on multicore architectures, J. Comput. Phys. 288 (2015) 1–18.
[62] C. Bernier, M. Gazzola, R. Ronsse, P. Chatelain, Simulations of propelling and energy harvesting articulated bodies via vortex particle-mesh methods, J. Comput. Phys. 392 (2019) 34–55.
[63] M. Gazzola, B. Hejazialhosseini, P. Koumoutsakos, Reinforcement learning and wavelet adapted vortex methods for simulations of self-propelled swimmers, SIAM J. Sci. Comput. 36 (2014) B622–B639, https://doi.org/10.1137/130943078.
[64] M. Gazzola, C. Mimeau, A. Tchieu, P. Koumoutsakos, Flow mediated interactions between two cylinders at finite re numbers, Phys. Fluids 24 (2012) 043103, https://doi.org/10.1063/1.4704195.
[65] G. Lorieul, Development and validation of a 2D Vortex Particle-Mesh method for incompressible multiphase flows, Ph.D. thesis, UCL-Université Catholique de Louvain, 2018.
[66] J.D. Eldredge, T. Colonius, A. Leonard, A vortex particle method for two-dimensional compressible flow, J. Comput. Phys. 179 (2002) 371–399.
[67] P. Parmentier, G. Winckelmans, P. Chatelain, A vortex particle-mesh method for subsonic compressible flows, J. Comput. Phys. 354 (2018) 692–716.
[68] G. Winckelmans, A. Leonard, Contributions to vortex particle methods for the computation of three-dimensional incompressible unsteady flows, J. Comput. Phys. 109 (1993) 247–273.
[69] P. Ploumhans, G. Winckelmans, Vortex methods for high-resolution simulations of viscous flow past bluff bodies of general geometry, J. Comput. Phys. 165 (2000) 354–406.
[70] T. Engels, D. Kolomenskiy, K. Schneider, J. Sesterhenn, Two-dimensional simulation of the fluttering instability using a pseudospectral method with volume penalization, Comput. Struct. 122 (2013) 101–112.
[71] A.F. Bower, Applied Mechanics of Solids, CRC Press, 2009.
[72] D. Rossinelli, M. Bergdorf, G.-H. Cottet, P. Koumoutsakos, Gpu accelerated simulations of bluff body flows using vortex particle methods, J. Comput. Phys. 229 (2010) 3316–3333.
[73] G. Carbou, P. Fabrie, et al., Boundary layer for a penalization method for viscous incompressible flow, Adv. Differ. Equ. 8 (2003) 1453–1480.
[74] P. Angot, C.-H. Bruneau, P. Fabrie, A penalization method to take into account obstacles in incompressible viscous flows, Numer. Math. 81 (1999) 497–520.
[75] C. Bost, G.-H. Cottet, E. Maitre, Convergence analysis of a penalization method for the three-dimensional motion of a rigid body in an incompressible viscous fluid, SIAM J. Numer. Anal. 48 (2010) 1313–1337.
[76] P. Angot, G. Carbou, V. Péron, Asymptotic study for Stokes–Brinkman model with jump embedded transmission conditions, Asymptot. Anal. 96 (2016) 223–249.
[77] K. Kamrin, J.-C. Nave, An Eulerian approach to the simulation of deformable solids: application to finite-strain elasticity, arXiv preprint, arXiv:0901.3799, 2009.
[78] T. Belytschko, W.K. Liu, B. Moran, K. Elkhodary, Nonlinear Finite Elements for Continua and Structures, John Wiley & Sons, 2013.
[79] J.-P. Pons, G. Hermosillo, R. Keriven, O. Faugeras, Maintaining the point correspondence in the level set framework, J. Comput. Phys. 220 (2006) 339–354.

[80] A. Koopman, H.J. Geijselaers, K. Nilsen, P. Koenis, Numerical flow front tracking for aluminium extrusion of a tube and a comparison with experiments, Int. J. Mater. Forming 1 (2008) 423–426.

[81] G.-H. Cottet, E. Maitre, T. Milcent, Eulerian formulation and level set models for incompressible fluid-structure interaction, Modél. Math. Anal. Numér. 42 (2008) 471–492.

[82] D.I. Levin, J. Litven, G.L. Jones, S. Sueda, D.K. Pai, Eulerian solid simulation with contact, ACM Trans. Graph. 30 (2011) 1–10.

[83] T. Dunne, An Eulerian approach to fluid–structure interaction and goal-oriented mesh adaptation, Int. J. Numer. Methods Fluids 51 (2006) 1017–1039.

[84] T. Milcent, E. Maitre, Eulerian Model of Immersed Elastic Surfaces with Full Membrane Elasticity, 2016.

[85] C.H. Rycroft, C.-H. Wu, Y. Yu, K. Kamrin, Reference map technique for incompressible fluid-structure interaction, arXiv preprint, arXiv:1810.03015, 2018.

[86] P. Nardinocchi, L. Teresi, On the active response of soft living tissues, J. Elast. 88 (2007) 27–39.

[87] Y. Fan, J. Litven, D.K. Pai, Active volumetric musculoskeletal systems, ACM Trans. Graph. 33 (2014) 152.

[88] I. Kataoka, M. Ishii, A. Serizawa, Local formulation and measurements of interfacial area concentration in two-phase flow, Int. J. Multiph. Flow 12 (1986) 505–529.

[89] R. Hockney, J. Eastwood, Computer Simulation Using Particles, CRC Press, 1989.

[90] P. Chatelain, P. Koumoutsakos, A Fourier-based elliptic solver for vortical flows with periodic and unbounded directions, J. Comput. Phys. 229 (2010) 2425–2431.

[91] J.T. Rasmussen, G.-H. Cottet, J.H. Walther, A multiresolution remeshed vortex-in-cell algorithm using patches, J. Comput. Phys. 230 (2011) 6742–6755.

[92] M.M. Hejlesen, P. Koumoutsakos, A. Leonard, J.H. Walther, Iterative Brinkman penalization for remeshed vortex methods, J. Comput. Phys. 280 (2015) 547–562.

[93] T. Gillis, G. Winckelmans, P. Chatelain, An efficient iterative penalization method using recycled Krylov subspaces and its application to impulsively started flows, J. Comput. Phys. 347 (2017) 490–505.

[94] L. Hume, P. Poncet, A velocity-vorticity method for highly viscous 3d flows with application to digital rock physics, J. Comput. Phys. 425 (2021) 109910.

[95] X.-D. Liu, S. Osher, T. Chan, et al., Weighted essentially non-oscillatory schemes, J. Comput. Phys. 115 (1994) 200–212.

[96] C.-W. Shu, S. Osher, Efficient implementation of essentially non-oscillatory shock-capturing schemes, II, in: Upwind and High-Resolution Schemes, Springer, 1989, pp. 328–374.

[97] S.E. Hieber, P. Koumoutsakos, A Lagrangian particle method for the simulation of linear and nonlinear elastic models of soft tissue, J. Comput. Phys. 227 (2008) 9195–9215.

[98] D. Kolomenskiy, K. Schneider, A Fourier spectral method for the Navier–Stokes equations with volume penalization for moving solid obstacles, J. Comput. Phys. 228 (2009) 5687–5709.

[99] J. Monaghan, Extrapolating B splines for interpolation, J. Comput. Phys. 60 (1985) 253–262.

[100] J.-M. Etancelin, P. Moonen, P. Poncet, Improvement of remeshed Lagrangian methods for the simulation of dissolution processes at pore-scale, Adv. Water Resour. 146 (2020) 103780.

[101] S. Ii, K. Sugiyama, S. Takeuchi, S. Takagi, Y. Matsumoto, An implicit full Eulerian method for the fluid–structure interaction problem, Int. J. Numer. Methods Fluids 65 (2011) 150–165.

[102] J.B. Freund, Numerical simulation of flowing blood cells, Annu. Rev. Fluid Mech. 46 (2014) 67–95.

[103] B.S. Massey, J. Ward-Smith, Mechanics of Fluids, vol. 1, CRC Press, 1998.

[104] R. Larson, D. Mead, The Ericksen number and deborah number cascades in sheared polymeric nematics, Liq. Cryst. 15 (1993) 151–169.

[105] P.J. Roache, Code verification by the method of manufactured solutions, J. Fluids Eng. 124 (2002) 4–10.

[106] T. Parthasarathy, Y. Bhosale, M. Gazzola, A simple, rigorous benchmark for fully coupled flow–structure interaction algorithms, arXiv:2011.09453, 2020.

[107] A. Robinson-Mosher, C. Schroeder, R. Fedkiw, A symmetric positive definite formulation for monolithic fluid structure interaction, J. Comput. Phys. 230 (2011) 1547–1566.

[108] M. Bar-Lev, H. Yang, Initial flow field over an impulsively started circular cylinder, J. Fluid Mech. 72 (1975) 625–647.

[109] J. Stuart, Double boundary layers in oscillatory viscous flow, J. Fluid Mech. 24 (1966) 673–687.

[110] A. Bertelsen, A. Svardal, S. Tjøtta, Nonlinear streaming effects associated with oscillating cylinders, J. Fluid Mech. 59 (1973) 493–511.

[111] T. Parthasarathy, Viscous streaming-enhanced inertial particle transport, Master's thesis, University of Illinois at Urbana-Champaign, 2018, https://www.ideals.illinois.edu/handle/2142/102963.

[112] T. Parthasarathy, F.K. Chan, M. Gazzola, Streaming-enhanced flow-mediated transport, J. Fluid Mech. 878 (2019) 647–662.

[113] N. Riley, On a sphere oscillating in a viscous fluid, Q. J. Mech. Appl. Math. 19 (1966) 461–472.

[114] C. Kotas, M. Yoda, P. Rogers, Visualization of steady streaming near oscillating spheroids, Exp. Fluids 42 (2007) 111–121.

[115] Y. Bhosale, Effects of shape geometry in viscous streaming, Master's thesis, University of Illinois at Urbana-Champaign, 2019, https://www.ideals.illinois.edu/handle/2142/106498.

[116] Y. Bhosale, T. Parthasarathy, M. Gazzola, Shape curvature effects in viscous streaming, J. Fluid Mech. 898 (2020) A13, https://doi.org/10.1017/jfm.2020.404.

[117] D. Wang, J. Tarbell, Nonlinear analysis of flow in an elastic tube (artery): steady streaming effects, J. Fluid Mech. 239 (1992) 341–358.

[118] P. Orlandi, Vortex dipole rebound from a wall, Phys. Fluids A, Fluid Dyn. 2 (1990) 1429–1436.

[119] I. Ramiere, P. Angot, M. Belliard, A fictitious domain approach with spread interface for elliptic problems with general boundary conditions, Comput. Methods Appl. Mech. Eng. 196 (2007) 766–781.

[120] B. Kadoch, D. Kolomenskiy, P. Angot, K. Schneider, A volume penalization method for incompressible flows and scalar advection–diffusion with moving obstacles, J. Comput. Phys. 231 (2012) 4365–4383.

[121] N.A. Valluvan, Development of a thermal flow solver using Remeshed Vortex Methods, Master's thesis, University of Illinois at Urbana-Champaign, 2018, https://www.ideals.illinois.edu/handle/2142/101555.

[122] D. Russell, Z.J. Wang, A Cartesian grid method for modeling multiple moving objects in 2d incompressible viscous flow, J. Comput. Phys. 191 (2003) 177–205.

[123] H. Nakamura, T. Igarashi, Variation of Nusselt number with flow regimes behind a circular cylinder for Reynolds numbers from 70 to 30 000, Int. J. Heat Mass Transf. 47 (2004) 5169–5173.

[124] S. Turek, J. Hron, M. Razzaq, H. Wobker, M. Schäfer, Numerical benchmarking of fluid-structure interaction: a comparison of different discretization and solution approaches, in: Fluid Structure Interaction II, Springer, 2011, pp. 413–424.

[125] S. Xu, Z.J. Wang, An immersed interface method for simulating the interaction of a fluid with moving boundaries, J. Comput. Phys. 216 (2006) 454–493.

[126] C. Jiang, J.-Y. Yao, Z.-Q. Zhang, G.-J. Gao, G. Liu, A sharp-interface immersed smoothed finite element method for interactions between incompressible flows and large deformation solids, Comput. Methods Appl. Mech. Eng. 340 (2018) 24–53.

[127] J. Towns, T. Cockerill, M. Dahan, I. Foster, K. Gaither, A. Grimshaw, V. Hazlewood, S. Lathrop, D. Lifka, G.D. Peterson, et al., Xsede: accelerating scientific discovery, Comput. Sci. Eng. 16 (2014) 62–74.